ABSTRACT

Title of dissertation: STOCHASTIC AND DETERMINISTIC DYNAMICS IN A SEMICONDUCTOR LASER WITH OPTICAL FEEDBACK

William Ray, Doctor of Philosophy, 2006

Dissertation directed by: Professor Rajarshi Roy
Department of Physics

Semiconductor lasers have been widely utilized in optical communications and optical data storage. However, in many important applications a small amount of the output light may be reflected back into the laser cavity resulting in large intensity fluctuations and a broadened laser linewidth. Here we experimentally and numerically characterize the subtle influence that spontaneous emission in the laser cavity has on shaping the instabilities produced by the time-delayed optical feedback from external reflections.

In the first experiment, we estimate the relative role played by deterministic and stochastic influences in the semiconductor laser at high injection currents under the influence of reflective feedback over a large range of feedback strengths. An empirical mode decomposition method is utilized to provide a physically significant definition of the Hilbert phase. Hurst exponent measurements of the Hilbert phase fluctuations show a clear transition from regular Brownian motion to fractional Brownian motion as the amplitude of coherent feedback is incremented in the experiment and model equations.

At lower injection currents noise is believed to play a much more crucial role in the intensity dropout dynamics witnessed by the system. In a second experiment we adapt a methodology commonly used to evaluated escape phenomena in the theory of large fluctuations to elicit deterministic features shared by many dropouts in an experimental an simulated intensity time series. The optimal path of dropout derived from this analysis demonstrates epochs both before and after the dropout where the system dynamics exhibits a chaotic itinerancy between external cavity lasing modes supported by the system.

Finally, we numerically investigate the role of additive noise in the selection of a chaotic instability supported by the semiconductor laser with time-delayed optical feedback for different parameter settings. We find that a single instability is preferred by the system over a larger region of the parameter space as the amplitude of the noise term is increased in the model equations. An experimental characterization of this stability region serves as a sensitive indicator of the amount of Langevin noise relevant in numerically describing stochastic influences present in the evolution of the light dynamics.

STOCHASTIC AND DETERMINISTIC DYNAMICS IN A SEMICONDUCTOR LASER WITH OPTICAL FEEDBACK

by

William Ray

Dissertation submitted to the Faculty of the Graduate School of the
University of Maryland, College Park in partial fulfillment
of the requirements for the degree of
Doctor of Philosophy
2006

Advisory Committee:
Dr. Rajarshi Roy, Chair/Advisor
Dr. Parvez N. Guzdar
Dr. Wolfgang Losert
Dr. Thomas Antonsen
Dr. Brian Hunt

ACKNOWLEDGEMENTS

Many individuals have contributed greatly to the ideas and progress of the research presented in this dissertation.

My advisor Dr. Rajarshi Roy has guided my education in the last four years more than anyone else. He has motivated my development of how to approach research problems with a cool head and a rapt attention to detail. I want to thank Dr. Parvez Guzdar for many fruitful discussions on the dynamics of semiconductor lasers and the subtleties involved in simulating them. I also would like to thank Dr. Ira Schwartz who has largely contributed to my understanding of stochastic and delay-differential systems.

Many aspects of the research were greatly enhanced by discussions with Dr. Atsushi Uchida, Dr. Wing-Shun Lam, Dr. Fabien Rogister, Dr. Leah Chock and Dr. Alexandra Landsman. I especially want to extend thanks to Yanne Chembo. Interactions with graduate students and my labmates Major Tony Franz, Dr. Beth Dakin, Dr. Min-Young Kim, and Dr. Bhaskar Kubchandani has provided a constant supply of inspiration and entertainment throughout the past few years. Crucial contributions to the experiments were made by undergraduate students Nathan Karst and Bethany Adams, in particular, as well as Jed Ziegler and Clinton Rebello.

I owe a large debt of gratitude to my parents Bill and Lucy Ray. You have both greatly shaped my view of life and guided me to where I am today. I finally want to extend appreciation to my wife Heather. Your loving support was responsible for keeping me sane throughout graduate school and this thesis would not have been possible without you.

TABLE OF CONTENTS

LIST OF FIGURES

Chapter 1

Introduction

Through the process of stimulated emission, a photon with the correct energy will induce an excited atom to emit a similar photon with identical phase, frequency, and direction of propagation. The first coherent source of radiation was produced by Townes and Shawlow in 1954, where they induced emission in the microwave regime with ammonia molecules. Four years later they published a landmark theoretical paper outlining how light may be amplified for infrared and optical frequencies [1]. The first laser to emit in the visible spectrum was soon developed by Maiman at Hughes Research Laboratories using a ruby crystal as the gain medium and a helical photographic strobe lamp as the power source [2]. While many materials have been utilized to generate coherent emission, the semiconductor laser, first discovered in 1962 [3, 4, 5, 6], accounts for 99.8% of the lasers sold in the world market [7]. Advances in fabrication technology have allowed the construction of small efficient semiconductor lasers which may be easily integrated with electronics at a low cost. Although they are often used as pump source for other lasing systems, the spectral content of semiconductor lasers permits information to be impressed on the light generated by modulation of the current powering the laser diode. As a result, these lasers are widely utilized for optical data storage and especially communication over optical fibers at the key telecommunications wavelengths of 1.3 μm and 1.55 μm.

Dispersion in the fiber is negligible at 1.3 μm and the loss in the fiber reaches a minimum at 1.55 μm [8]

However, the light dynamics of a semiconductor laser may be strongly influenced by outside perturbations introduced into the system. Even small influences may strongly affect their performance in communications systems. In this Chapter we describe some characteristics of semiconductor lasers and discuss instabilities which may result in the light dynamics when a powerful perturbation that the laser is most sensitive to, the re-injection of time-delayed optical feedback from a distant reflector, is introduced into the active medium of the laser diode. A consideration of the phenomena that result motivates the aim of this study, which is to analyze the effect that noise has in influencing the global dynamics witnessed in the semiconductor laser.

1.1 Semiconductor Lasers

1.1.1 Operating Principles

As with any realization of coherent emission, three requirements are necessary in order for semiconductor material to lase: (1) a medium which allows stimulated emission, (2) a source providing population inversion to the system, and (3) the construction of a cavity to locally confine the generated light so that lasing conditions may persist. Semiconductors are based on p-n junctions of semiconductor materials. In materials such as BaAl, GaInN the separation of valence and conduction bands on the order of a few eV, which is comparable to energy of photons in the visible

spectrum. A range of materials have been developed to produce wavelengths over a wide spectrum from 0.1 μm to 3 μm. The energy band gap of the lasing medium may additionally be adjusted when the laser is manufactured using strain [9].

In semiconductors the gain is achieved via carriers, which consist of an electron-hole pair, where the electron lies in bottom of the conduction band and the hole (absence of electron) resides near the top of the valence band. In thermodynamic equilibrium, the electrons and holes distributed over a quasi-continuum range of energies described by Fermi-Dirac statistics and may be described by a density of states. The carriers serve as a source for stimulated emission, as photons may induce radiative recombination of the electron and hole producing a photon with identical characteristics. However, the carriers may spontaneously recombine to form photons that do not share characteristics with the coherent state. In addition, absorbtion of light in the gain medium may produce carriers and various mechanisms for non-radiative recombination due to material defects are present as well. Nonradiative depletion of carriers also occurs in Auger recombination, where an electron and hole recombine but the energy of this transition is used to further excite an electron [8].

It is clear that with many competing recombination and absorption processes in the gain medium, the rate of stimulated emission is extremely small. Many carriers must be available in a small region in order for stimulated emission to dominate the light dynamics. Laser action arises when a sufficient density of carriers are injected into a gain medium from an electrical contact. For very small injection currents, the light is primarily produced by spontaneous emission, as a majority of the photons are absorbed before they may initiate stimulated emission with remain-

ing carriers. When the injection current is tuned high enough such that enough light is generated to overcome absorption, then the material is *transparent*. Upon a further increase of injected charge carriers, stimulated emission may begin but the coherent light produced is attenuated as it travels through the material. Dissipation processes in the gain medium and losses of photons out of the injected region must be compensated by a further increase of the injection current. Once these are overcome, lasing threshold is reached and stimulated emission will dominate the light output processes producing a coherent light source of light. Further increases of the injection current at this point translate into a proportional increase of the output intensity of the laser (losses along the direction of propagation), as the number of carriers in the medium are clamped to the amount produced at the lasing threshold.

As discussed above, the electrons and holes must be densely concentrated into a small region to generate enough stimulated transitions for sufficient light output. This localization is commonly achieved in practice with the use of a heterostructure. This arrangement is depicted in Fig. 1.1. The region where gain is achieved, the active layer, is sandwiched between two semiconductor materials which each possess a wider band-gap. This feature more efficiently confines charge carriers injected into the active layer when forward bias is applied so the lasing threshold may be reached for lower levels of the injection current. Furthermore, the potential barrier created by the band-gap difference allows the thickness of the active layer to be tightly controlled.

The cladding layers provide a useful method to confine the carriers and enhance the population inversion. Once coherent light is generated, it is also important to

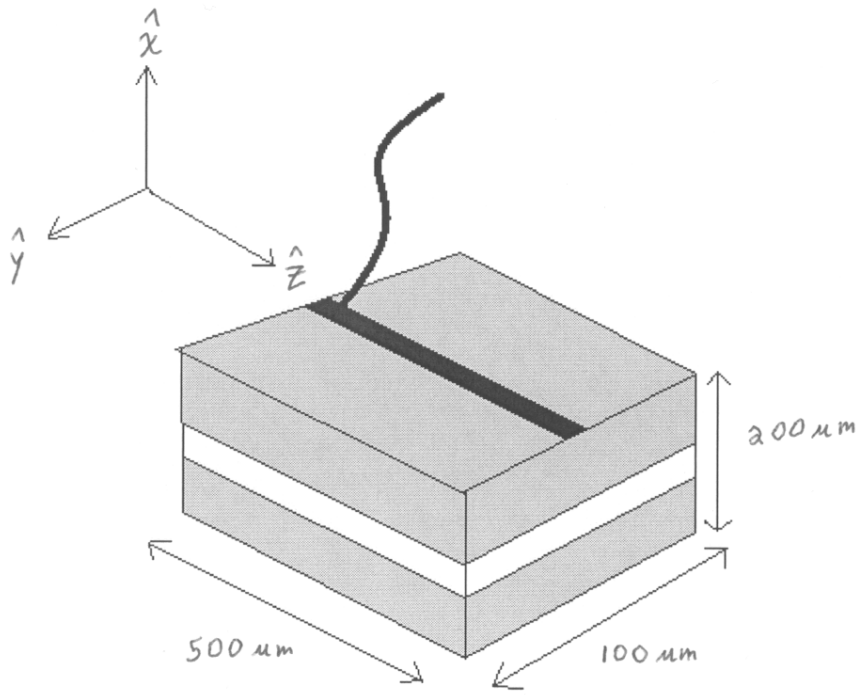

Figure 1.1: A schematic of the heterostructure which dramatically increases lasing efficiency. The cladding layers effectively confine the carriers in the active region due to a larger band-gap of the supporting materials. Gradations in the refractive index in the active layer (perpendicular to the y direction) aid in concentrating as much light as possible along the direction of propogation (z direction).

retain a good portion of the optical field within the active layer to promote further stimulated emission. In an edge-emitting laser the direction of propagation is parallel with the thin active layer of the heterostructure. A Fabry-Perot resonant cavity is comprised of polished facets which are established by cleaving the semiconductor laser along the crystal plane. Standing waves in the cavity form the longitudinal modes available for lasing emission. The reflectivity of the facets is generally only around 30%, much lower than most other lasing mediums with mirrors reflecting near all of the light in the gain medium. The reflectivity of one facet is often coated with a dielectric material to establish a single output for the light. The cladding layers confining the carriers are chosen to have a lower index of refraction then the active layer which serves to concentrate the optical field in the active medium (x direction). The current is injected along a thin stripe parallel to the desired direction of propagation (z direction) as shown in Fig. 1.1. The gain applied along this stripe can serve to localize the gain in the active medium, a process known as gain-guiding, but lower threshold injection currents may be achieved by introducing a variation of the refractive index along the plane of the active medium which is perpendicular to the direction of propagation.

When the laser is pumped beyond lasing threshold, the optical spectrum exhibit single or multi-mode emission which may be dependent on the temperature and level of injection current [10]. Distributed feedback lasers and distributed Bragg reflectors use a grating along the direction of propagation to establish the oscillation of a single longitudinal mode. The polarization direction is determined by the cladding structure (y direction) and the semiconductor will often emit with a TE

mode. The TM mode is possible but the TE is more likely because of its higher reflectivity from the polished facets [11].

1.1.2 Dynamic and Stochastic Characteristics

Under lasing conditions a semiconductor laser will emit at a constant power output determined by the injection current level. Spontaneous emission results in fluctuations of the intensity as well as the phase. However, the phase is further affected a short time later by the instantaneous change in the field intensity. The delayed change in the phase is particularly pronounced in semiconductor lasers. A fine balance exists between the carrier number and the electric field in the resonator so that a fluctuation in the intensity results in a corresponding change in the carrier number. The interplay between these two variables is manifested through the relaxation oscillations

$$f_{RO} = \frac{1}{2}(\frac{1}{\tau_e \tau_{ph}})(\frac{I}{I_{th}} - 1)^{\frac{1}{2}}. \tag{1.1}$$

determined by the characteristic lifetimes of the carrier number τ_e and photons τ_{ph} as well as the level of injection current I with respect to solitary lasing threshold I_{th}. In a semiconductor laser the change in the gain of the optical field with respect to a change in the carrier number (the imaginary part of the refractive index) is overshadowed by the deviation which occurs in the real part of the refractive index due to a carrier change [12]. The ratio of the change in the real part of the refractive index to the change in the gain may be characterized by the line-width enhancement factor α, also known as the phase-amplitude coupling coefficient. This parameter

is normally much below unity for most lasers but generally takes a value of $3-6$ in semiconductor lasers. As its name implies the line-width enhancement factor strongly affects the spectral purity of the laser emission by widening the emission spectrum by a factor of $1+\alpha^2$.

1.2 Consequences of Coherent Optical Feedback

The short time scale of the relaxation oscillations (less than 1 ns) in a semiconductor laser make it an attractive candidate for modulation in communications systems. However, due to the low reflectivity of the facets comprising the Fabry-Perot cavity, a semiconductor laser is sensitive to outside perturbations from the environment. When an external optical field is injected into the cavity or the laser receives time-delayed light from a reflection back into the active medium, complicated dynamics may be exhibited in the light dynamics. Here we focus on the dynamical consequences which result from the introduction of coherent optical feedback back into the laser cavity.

Time-delayed feedback is prevalent in many physical processes and is a relevant element which must be considered in the accurate characterization of ecological and biological systems. Feedback loops are found in the finite transmission of neural spikes and in many of regulation processes within the body to establish homeostasis [13]. The delay may appear as a discrete re-injection of a signal into a system or its influence may be distributed over a finite time interval. In either case, the presence of delayed information in the system will often cause complex behavior

and increase the dimensionality available to motions in the system [14]. Since the continuous interval of the delay line must be specified in such a system, the phase space is essentially rendered infinite-dimensional [15].

We mention that time delays may additionally be manifested in a semiconductor laser through incoherent optical feedback [16] or through optoelectronic feedback via a time-delayed modulation of the injection current [17]. In many situations of practical interest the feedback is generated by the reflection of a coherent optical field back into the resonant cavity comprising the laser diode, and many studies have focused on understanding the dynamics of this feedback source. While early interest in the effects of reflective feedback in semiconductor lasers stemmed from observations of enhanced noise properties, the focus later shifted to view the deleterious effects of the perturbation as a nonlinear dynamical phenomenon when chaotic signatures were recognized in observations of the system [18].

Tkach and Chraplyvy [19] partitioned the experimental observations caused by feedback into five regimes dependent on the amount of feedback which is transmitted back into the laser cavity. For extremely small feedback strengths the line-width of the laser diode may narrow [20, 21] or broaden [22] as a result of the phase shift incurred during the finite propagation of the light through the passive external cavity. For slightly larger feedback strengths longitudinal mode-hopping may be induced or the laser may lock to the mode with the minimum line-width.

Even though desirable spectral results may be produced with a small amount of feedback, over a large range of feedback strengths from $\sim 10^{-4}$ to 10^{-1} the line-width of the laser may dramatically enlarge from about 10 MHz to well over 20 GHz.

It is in this regime where nonlinear effects dominate the light dynamics and are most problematic for implementations of semiconductor lasers in practice. A vast number of studies have traced routes to chaotic output in the laser for increasing feedback strengths and various descriptions of the underlying dynamics have been proposed. The physically intuitive Lang-Kobayashi delay-differential equations [23] are widely regarded to most accurately capture the increased line-width and large amplitude fluctuations witnessed in experimental observations. Investigations of this model predict that the light dynamics are the result of mode-hopping among a large number of peripheral modes formed by the feedback cavity.

1.3 Chaotic Itinerancy

Chaotic itinerancy (CI) has recently been proposed as a ubiquitous phenomenon in a variety of high-dimensional dynamical systems, and is generally recognized as itinerant switching between low-dimensional attractors via high-dimensional chaos [24]. Experiments and numerical models of nonlinear coupled oscillators [25] and systems with time-delayed feedback [26], in particular, have contributed largely to the characterization of this dynamic mechanism. Optical media under the influence of delayed feedback have served as exemplary systems for studying manifestations of CI [27], and itinerant motion has been found to be relevant in describing the dynamical behavior of photorefractive cells [28] and laser systems exhibiting multimode oscillations [29].

For moderate levels of reflective feedback, the light dynamics of a semiconduc-

tor laser have numerically been shown to itinerate across hundreds of external cavity modes for a wide range of injection currents. This phenomenon is traditionally characterized in simulations of the Lang-Kobayashi equations for the complex electric field and population inversion. Streak camera measurements of the light dynamics on very short time scales have provided indirect confirmation of the deterministic scenario of LFF predicted from the numerical model [67]. Hilbert phase information extracted from filtered intensity measurements has previously demonstrated external cavity mode shifts [31].

1.4 Outline

Although a semiconductor laser may wander between hundreds of external cavity modes as a result of coherent optical feedback, two behaviors have been observed to emerge in the global dynamics of the system. The Lang-Kobayashi equations predict that each dynamical state shares the same backbone of attracting states. As we will demonstrate in the following chapter, the determining factor of the global dynamics exhibited by the system lies with the transitions which are observed to occur *between* the individual external cavity lasing modes.

The purpose of this study is to gain a more complete understanding of the factors which contribute to the intermode interactions of the dynamical states in this system. In particular, we focus on the role that noise plays in dictating the transition characteristics of the system which ultimately determine the global dynamics assumed in the light dynamics of the semiconductor laser. After a brief

consideration of the dynamics of the Lang-Kobayashi model in Chapter 2, three investigations are conducted with the motivation of quantitatively elucidating the influence of noise in this high-dimensional system.

1.4.1 Hurst Exponent Measurements

When both noise and deterministic feedback yield similar signatures in traditional spectral and dynamical measurements, how can we discern the effects of each on the light output. In Chapter 3, the phase dynamics of a semiconductor laser with optical feedback is studied by construction of the Hilbert phase from its experimentally measured intensity time series. The Hurst exponent [32] is evaluated for the phase fluctuations and grows from 0.5 to ~ 0.7 (indicating fractional Brownian motion [33]) as the feedback strength is increased. A comparison with numerical computations based on a delay-differential equation model shows excellent agreement and reveals the relative roles of spontaneous emission noise and deterministic dynamics for different feedback strengths.

1.4.2 Chaotic Itinerancy near Solitary Lasing Threshold

In Chapter 4 we report a direct experimental observation of chaotic itinerancy in simultaneous measurements of the light intensity and voltage fluctuations of a laser diode exhibiting low-frequency fluctuations. The distribution of trajectories leading up to (following) an intensity dropout is computed from the experiment and reveals the presence of itinerant mechanisms before (after) dropout initiation. Here

we extract itinerant motions significant to a large number of dropouts by adopting a methodology [34] commonly used to study escape dynamics in the theory of large fluctuations. The distribution of trajectories leading to escape from a metastable state generally displays a distinct peak, known as the optimal path, indicating how the system is most likely to move.

In the context of large fluctuations, the motion and variance of this optimal path gives insight to the potential barrier crossed during activated escape [35]. For the purposes of our study, the optimal path reveals epochs before and after the dropout where the system dynamics is dominated by high-dimensional transitions between external cavity modes. A phase space reconstruction of the trajectory for the optimal path of motion illustrates sudden shifts between low-dimensional attractor ruins and is shown to correspond to simulations of the laser intensity and carrier number.

1.4.3 Noise-Induced Selection of the Laser Dynamics

Noise is an inevitable element which must be considered in any experimental realization, and a number of studies have focused on the effect of stochastic driving in a variety of nonlinear systems. In many circumstances noise may have a positive influence on the trajectory of a dynamical system. Two common manifestations are found in stochastic resonance [36], where the response of a periodic driving signal is enhanced with the appropriate addition of noise, and coherence resonance [37], where input noise regularizes the occurence of large fluctuations in

an excitable system. More recently, the role of noise has been studied in systems exhibiting a large number of attractors. Even a small amount of injected noise may dramatically affect the stability of individual attractors in a multi-stable system, particulary when the basins of the constituent attractors are riddled or possess a fractal boundary. As a result, multistability may be enhanced in a system [38] or the noise may induce the trajectory to transiently wander between attractors. When the noise is strong enough to induce attractor-hopping, studies of GCMs [39] and a kicked rotor [40] have revealed noise-induced attractor selection. The trajectory is preferentially guided by noise towards weak attractors of the system, and the attractor visited most often stongly depends on the level of noise.

In situations where the underlying system possesses a large number of degrees of freedom, transient switching between multiple attractors may be witnessed *without* the influence of a stochastic term. Even though the system never settles on a single attractor, dynamical states in these systems may be globally defined by the set of transitions observed to occur between attractor ruins.

In Chapter 5 we examine the role of additive noise in selecting the dynamical states observed in a semiconductor laser with time-delayed optical feedback. We quantitatively characterize an intermittency between the two dominant dynamical states over a wide range of a system parameter for different levels of Langevin noise. As higher levels of noise are introduced into the system, the system preferentially selects one of the dynamical states for a larger span of the parameter, preventing the onset of intermittency. The characteristic scaling associated with the intermittent transition is characterized experimentally and is shown to exhibit a sensitive

dependence to the level of noise in the model equations.

Chapter 2

Dynamics in the Presence of Optical Time-Delayed Feedback

The Lang-Kobayashi model [23] has been the paradigmatic model for studying instabilities in semiconductor lasers under the influence of optical feedback due to a widespread success in describing experimental observations over a wide range of parameters. The model is simply formed by combining the standard semiclassical rate equations, where light is treated classically from a consideration of Maxwell's equations in a cavity in concert with a quantum treatment of carriers, with a direct addition of a discrete injection of a time-delayed field. In this Chapter we introduce the Lang-Kobayashi model and focus on the formulation of two important parameters: the linewidth enhancement factor and the rate at which feedback is re-injected into the laser cavity. The contribution of each quantity has a profound influence on the dynamical states which are realized in the compound cavity system. The nonlinear characteristics are additionally discussed and we emphasize the importance of the interplay between individual attractors which are formed from steady-state solutions of the Lang-Kobayashi equations, as they ultimately govern the global behavior which is accessible experimentally.

2.1 The Lang-Kobayashi Equations

The single-mode Lang-Kobayashi equation for the complex electric field in a compound cavity consisting of the active gain medium (with internal round-trip time τ_{int} and the passive external resonator (round-trip time τ) follows below:

$$\frac{d}{dt}E(t)e^{i\omega_0 t} = [i\omega_N(n(t)) + \frac{1}{2}(G(n(t)) - \Gamma)]E(t)e^{i\omega_0 t} + \kappa E(t-\tau)e^{i\omega_0(t-\tau)}. \quad (2.1)$$

The slowly-varying envelope of the electric field is modulated rapidly by the solitary emission frequency ω_0. The first term on the right-hand side reflects the dependence of the longitudinal mode resonant frequency

$$\omega_N \equiv \frac{N\pi c}{\eta l_{int}} \quad (2.2)$$

on the carrier number n which, as discussed below, occurs via the refractive index η. The integer N defines which longitudinal mode is exhibited in the cavity, c is the light velocity, and l_{int} is the length of the laser diode cavity. The second term accounts for the balance between the gain amplification $G(n)$ due to stimulated emission and the attenuation of the light described the cavity decay rate $\Gamma = 1/\tau_{ph}$, where τ_{ph} is the lifetime of the photon. The photon losses stem from light exiting through the material layers and the polished facets of the resonant cavity. The direct addition of coherent optical feedback frames Eqn. 2.1 as a delay-differential equation.

The rate equation Eqn. 2.1 is coupled with the evolution of the carrier number

$$\frac{d}{dt}n(t) = \frac{J}{ed} - \frac{n(t)}{\tau_e} - G(n)|E(t)|^2. \quad (2.3)$$

The first term represents the injection rate per unit volume of the excited carriers in terms of the injection current density J, the electronic charge e, and the active layer thickness d. The carrier lifetime τ_e reflects the decay of the excited states as a result of the spontaneous recombination of electrons and holes as well as non-radiative recombination from defects and Auger recombination. The third term accounts for the depletion of the carriers due to stimulated emission. This equation additionally assumes that carrier diffusion is not relevant in describing the dynamics of the compound cavity, a reasonable assumption for the index-guided lasers realized in our experiments.

2.1.1 Phase-Amplitude Coupling

We now apply a linear approximation for the gain and refractive index to evaluate how changes in the carrier number affect the resonant frequency ω_N [12]. For small variations $\delta n(t) = n(t) - n_{th}$ of the carrier number around the solitary lasing threshold n_{th}, the refractive index may be described as

$$\eta(t) = \eta_{th} + \delta n \frac{\partial \eta}{\partial n}. \tag{2.4}$$

Plugging this relation into Eqn. 2.2 the longitudinal mode frequency assumes the form

$$\omega_N = \omega_{th} - \frac{\omega_{th}}{\eta_{th}}(\delta n \frac{\partial \eta}{\partial n}). \tag{2.5}$$

As the gain is similarly dependent on the number of carriers in the active layer, we may approximate the gain near threshold as

$$G(n) = G_{th} + \delta n \frac{\partial G}{\partial n}. \tag{2.6}$$

However, the threshold condition for the solitary laser requires the gain to match the photon losses in the cavity, hence $G_{th} = \Gamma$ and we may express δn as

$$\delta n = \frac{(G(n) - \Gamma)}{\frac{\partial G}{\partial n}}. \tag{2.7}$$

When this expression is utilized in Eqn. 2.6, then the resonant frequency relative to threshold reads as

$$(\omega_N - \omega_{th}) = \frac{\alpha(G(n) - \Gamma)}{2} \tag{2.8}$$

where

$$\alpha \equiv -\frac{2\omega_{th}}{\eta_{th}}(\frac{\frac{\partial \eta}{\partial n}}{\frac{\partial G}{\partial n}}) \tag{2.9}$$

is the phase-amplitude coupling which has important consequences in describing response characteristics and the line-width broadening observed in semiconductor laser dynamics. We substitute Eqn. 2.8 into the rate equation for the electric field Eqn. 2.1 and cancel out the rapidly oscillating exponential to obtain

$$\frac{d}{dt}E(t) = \frac{1}{2}(1 + i\alpha)G_n(n(t) - n_{th})E(t) + \kappa E(t - \tau)e^{i\omega_0(t-\tau)} \tag{2.10}$$

in terms the differential gain $G_n = \partial G/\partial n$ and deviation of the carrier density from threshold. From this representation of the Lang-Kobayashi field equation it is clear that α explicitly connects fluctuations in the amplitude to changes in the phase. As this factor enhances the line-width of the resonant frequency, we will later see that it additionally plays a substantial role in opening up compound cavity modes available to the system in the presence of optical feedback.

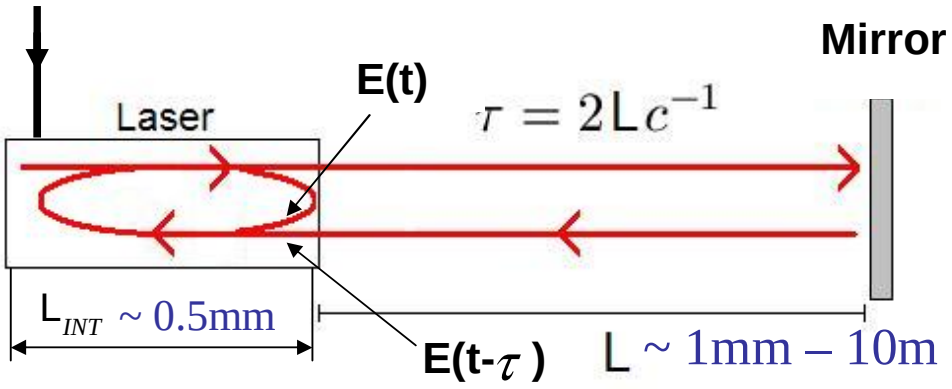

Figure 2.1: Schematic of the coherent addition between the optical field inside the laser cavity $E(t)$ reflected off the output facet with reflectivity r and the time-delayed light $E(t-\tau)$ re-entering the laser cavity. This process occurs at a rate $\tau_{int}^{-1} = 2L_{int}/c$ describing the round-trip time of the light within the gain medium.

2.1.2 Optical Feedback

The external cavity of the laser system is simply constructed by placing a mirror of reflectivity R at the desired distance l_{ext} from the front facet (with reflectivity r) of the laser diode. This distance defines the round-trip time in the passive external cavity $\tau = 2l_{ext}/c$. The amount of light re-injected after passing through the cavity is characterized by the coupling coefficient κ. The time delay additionally introduces a phase shift $e^{-i\omega_0\tau}$. We now reframe this coupling in terms of the losses suffered during the journey of the output through the external cavity. As shown in Fig. 2.1, at a rate of τ_{int}^{-1} the time-delayed light $E(t-\tau)$ reenters the laser diode at the front facet and meets with the field $E(t)$ which has just been reflected from within the active medium. Then the composite field $E'(t)$ heading towards the back facet takes the form

$$
\begin{aligned}
E'(t) &= E(t)\sqrt{r} + E(t-\tau)\sqrt{1-r}e^{-i\omega_0\tau/2}\sqrt{R}e^{-i\omega_0\tau/2}\sqrt{1-r} \\
&= \sqrt{r}E(t) + (1-r)\sqrt{R}E(t-\tau)e^{-i\omega_0\tau}. \qquad (2.11)
\end{aligned}
$$

From this equation we see that the time-delayed field transmits out of the cavity through the facet and picks up a phase shift of $e^{-i\omega_0\tau/2}$ on its way to the external reflector. After reflection, another phase shift is obtained and finally the field meets up with the light present in the cavity after a final transmission through the front facet. It follows that for each round trip undertaken by the light within the laser diode, the time-delayed field is injected with a phase shift $e^{-i\omega_0\tau}$ at a rate

$$\kappa = \frac{1-r}{\tau_{in}}\sqrt{\frac{R}{r}}. \qquad (2.12)$$

2.1.3 Spontaneous Emission

The effect of noise has not been considered so far in the model of the Lang-Kobayashi equations, yet as we will see in future chapters it has a profound influence on the dynamics of the model equations and its inclusion is important for an accurate representation of experimental observations. The primary source of noise is spontaneous emission in the amplitude and the phase dynamics of the light. Since the optical field is not quantized in the semiclassical treatment of the dynamics in the Lang-Kobayashi equations, the noise source may be represented by a complex Langevin noise current $F_E(t)$ described by Gaussian random numbers with zero mean $\langle F_E(t)\rangle = 0$ and a delta-correlation

$$\langle F_E(t)F_E^*(t')\rangle = R_{sp}\delta(t-t'). \qquad (2.13)$$

The number of spontaneous emission events which couple with the lasing mode are phenomenologically described by the Langevin noise amplitude R_{sp}.

We may numerically construct the Langevin noise current [42] at each time step dt in the integration of the model equations for each component of the complex electric field by calculating $F_E(t) = G_r(t) + iG_i(t)$, where

$$G_r = \sqrt{-2R_{sp}dt\log(u_1)}\cos(2\pi u_2), \tag{2.14}$$

$$G_i = \sqrt{-2R_{sp}dt\log(u_1)}\sin(2\pi u_2), \tag{2.15}$$

are Gaussian sources constructed from random numbers u_1 and u_2 drawn from a uniform distribution over the unit interval. A noise current $F_n(t)$ may also be considered in the rate equation for the carrier density to account for contributions of spontaneous emission and shot noise, but we will neglect it here as it does not have much impact on the dynamics in the presence of $F_E(t)$.

2.1.4 Normalized Equations

When we take into account the expressions for feedback (Eqn. 2.12) and fluctuations due to the Langevin noise, the rate equation for the optical field (Eqn. 2.10) now reads

$$\frac{d}{dt}E(t) = \frac{1}{2}(1+i\alpha)G_n(n(t)-n_{th})E(t) + \frac{1-r}{\tau_{in}}\sqrt{\frac{R}{r}}E(t-\tau)e^{i\omega_0(t-\tau)} + F_E(t). \tag{2.16}$$

In this form of the field equation the carrier number is evaluated with respect to its deviation from threshold. The rate equation for the carrier number may similarly

be rearranged by observing that, at solitary lasing threshold without feedback, the threshold current I_{th} may be directly calculated from the carrier number at threshold as $J_{th}/ed = I_{th}/e = n_{th}/\tau_e$. Using this relation and Eqn. 2.6, then Eqn. 2.3 may be expressed as

$$\frac{d}{dt}n(t) = \frac{I}{e} - (\frac{I_{th}}{e} - \frac{N_{th}}{\tau_e}) - \frac{n(t)}{\tau_e} - (G_{th} + G_n(n - n_{th}))|E(t)|^2. \tag{2.17}$$

After some rearrangement the rate equation of the carrier number reads as

$$\frac{d}{dt}n(t) = (P_I - 1)\frac{n_{th}}{\tau_e} - \frac{n - n_{th}}{\tau_e} - G_n(n - n_{th})|E(t)|^2 - \Gamma|E(t)|^2, \tag{2.18}$$

where $P_I = I/I_{th}$ is the normalized pump current with respect to threshold and $\Gamma = G_{th}$ represents the losses at threshold conditions.

In later chapters we will often utilize a normalized version of the Lang-Kobayashi equations [43],

$$\frac{dE}{dt} = (1 + i\alpha)nE(t) + \kappa E(t - \theta)e^{-i\omega_0\theta} + F_E(t), \tag{2.19}$$

$$\frac{dn}{dt} = \frac{1}{T}(p - n - (1 + 2n)|E|^2). \tag{2.20}$$

In this version of the delay-differential equations the parameters are scaled to the photon lifetime τ_{ph} and the field and carrier number are normalized to remove the differential gain. Here $E(t) = |E(t)|e^{i\phi(t)}$ is the normalized complex optical field and $n(t)$ is the difference in carrier number with respect to solitary lasing conditions. Also θ is the external cavity round trip time and ω_0 is the dimensionless solitary laser frequency; p is the dimensionless pump strength above threshold; $F'_E(t)$ is the Langevin noise term, with $\langle F_E(t)F_E(t')^*\rangle = R_{sp}\delta(t - t')$, where R'_{sp} is the

dimensionless spontaneous emission rate; T denotes the ratio between the decay time of photons in the laser cavity and the carrier recombination time.

All computations of the Lang-Kobayashi equations in this study are integrated using a fourth-order Runge-Kutta method [42]. In the following sections the steady state solutions of the normalized Lang-Kobayashi equations are evaluated.

2.2 Dynamics in the Presence of Optical Feedback

We assume that the stationary solutions of Eqns. 2.19 and 2.20 can be expressed as $E(t) = E_s e^{i\omega_s t}$ and $n(t) = n_s$. Additionally, the optical phase, defined from the slowly-varying envelope of the electric field $E(t) = A(t)e^{i\phi(t)t}$ with amplitude $A(t)$, is conveniently represented in the analysis by the introduction of the external cavity phase shift $\eta(t) = (\phi(t) - \phi(t-\theta))$ and the corresponding stationary solution $\eta \equiv \omega_s \theta$.

2.2.1 Solutions of the Lang-Kobayashi Equations

In the phase space of $|E(t)|^2$, $n(t)$, and $\eta(t)$, the fixed points of the system satisfy

$$\eta_s = -\kappa\theta\sqrt{1+\alpha^2} sin(\eta_s + \omega_0\theta + tan^{-1}\alpha), \tag{2.21}$$

$$n_s = -\eta cos(\eta_s + \omega_0\theta), \tag{2.22}$$

$$E_s^2 = \frac{p - n_s}{1 + 2n_s}. \tag{2.23}$$

$$\tag{2.24}$$

An immediate inspection of the above fixed points clearly shows that the trancendental equation for the external cavity phase shift determines the number and position of available fixed points. The intensity and carrier number follow directly from the solutions of Eqn. 2.21. When $C = \kappa\theta\sqrt{1+\alpha^2} < 1$, only one solution exists close to the solitary laser frequency. As the feedback strength is increased, new fixed points are created in pairs via a saddle-node bifurcation. The emergence of new fixed points, which may also be generated by increases in the external cavity round-trip time or the linewidth enhancement factor, can be visualized in the graphical solution of Eqn. 2.21 shown in Fig. 2.2.

A linear stability analysis of the fixed points [44] reveals that for every pair created, one may be identified as an *external cavity mode* (ECM) of the laser and the other is an inherently unstable saddle point (*antimode*). The ECMs shifted from the solitary laser frequency physically represent constructive interference between the external cavity and the optical field, while the antimodes correspond to destructive interference. Upon its inception, each new ECM is stable but suffers a Hopf bifurcation to periodic oscillations (relaxation oscillations become undamped) as the feedback level is incremented. At even higher levels of feedback the attractor present at each existing ECM follows a quasiperiodic route to chaos [45, 46]. Although this is the most common path for the emergence of chaotic emission, a period-doubling route has been observed when the relaxation oscillatons matched a harmonic of the external cavity round-trip time.

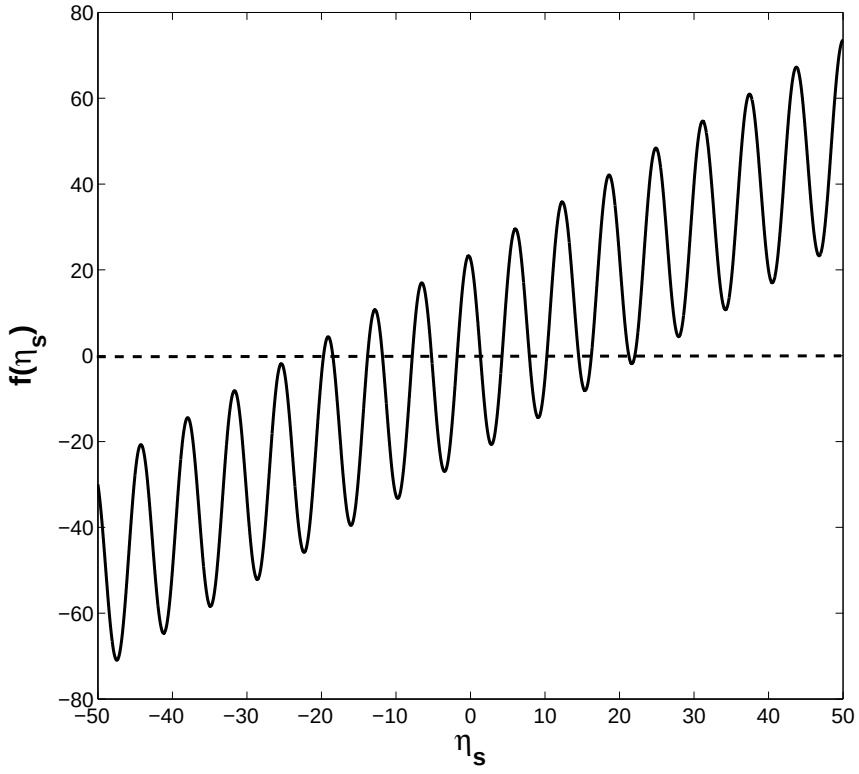

Figure 2.2: The fixed points of the Lang-Kobayashi equations satisy $f(\eta_s) = \eta_s + \kappa\theta\sqrt{1+\alpha^2}sin(\eta_s + \omega_0\theta + tan^{-1}\alpha) = 0$. New pairs are created when an increase in the amplitude penetrates the horizontal axis.

2.2.2 The Rise of Chaotic Itinerancy

If the amount of feedback is sufficiently low, multiple chaotic attractors coexist at the external cavity modes with separate basins of attraction. For moderate feedback strengths the time-dependent solutions are no longer confined to a local attractor surrounding each ECM and individual attractors begin to merge. The laser emission will transiently move along the unstable chain of attractor 'ruins' associated with the steady-state solutions, and the dynamics is said to exhibit a chaotic itinerancy. The antimodes play a substantial role in regulating the individual connections between ECMs.

The emergence of locally coupled attractor ruins is considered more concretely in Fig. 2.3 for computations of the Lang-Kobayashi equations without the inclusion of additive Langevin noise [47]. For a low level of feedback $\kappa = 0.003$, the time series of the external cavity phase shift in Fig. 2.3 (a) wanders around a single chaotic attractor. If the initial conditions are set close to other ECMs, spaced at intervals of 2π apart, the trajectory of the system will similarly be locally confined to the the nearby attractors (not shown). When the feedback is incremented to $\kappa = 0.005$, attractor-merging of the ECMs is evident as depicted in Fig. 2.3 (b). The duration spent near individual attractors will often fall close to a multiple of the external cavity round trip time, but at higher feedback strengths mode-hopping in the light dynamics may occur at a faster time-scale. In Fig. 2.3 (c) the mode-hopping becomes more frequent at a feedback level of $\kappa = 0.008$.

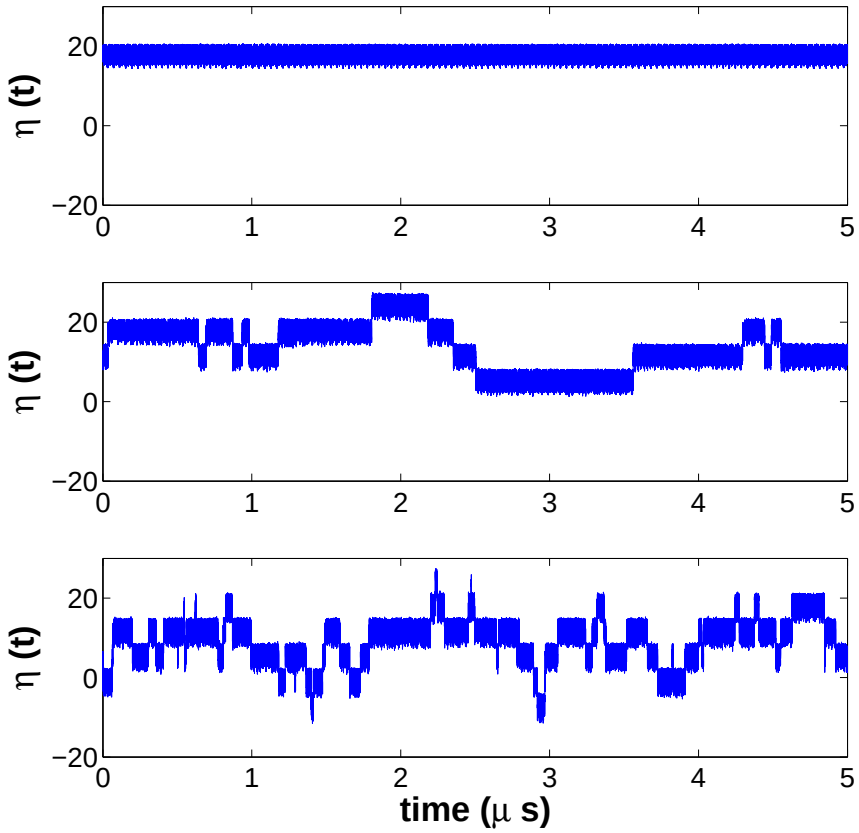

Figure 2.3: The dynamical interaction of the ECMs for feedback strengths of (a) $\kappa = 0.003$ (b) $\kappa = 0.005$ and (c) $\kappa = 0.008$. The ECMs are spaced 2π apart (with antimodes offset by π) and mode-hopping is seen to emerge for feedback levels higher than $\sim \kappa = 0.0043$.

2.2.3 Observed Dynamical States

At higher levels of feedback or in the presence of a long external cavity round-trip time (> 1 *ns*) *hundreds* of locally-coupled attractor ruins may participate in the dynamics. When a particular ECM is visited by the system, the trajectory of the system variables is highly localized around the ECM, but since the system never settles down the resulting dynamical state observed in the system must be typified by terms of the characteristic transitions which occur between the ECMs. The dynamics of these motions is traditionally viewed in the $(\eta(t), n(t))$ phase space, where the fixed points lie on a tilted ellipse [48]. In this representation the ECMs lie along the lower branch of the ellipse while the antimode comprise the upper branch. In addition to increasing the number of ECMs available to the system, the line-width enhancement factor defines the eccentricity of the ellipse and regulates the size of constituent attractors [49]. As discussed in the previous chapter, two dynamical states have been extinsively characterized in experiments and simulations over a wide range of system parameters.

When the laser dynamics exhibit low-frequency fluctuations (LFF) as depicted in the simulated intensity time trace in Fig. 2.4 (a), the system trajectory wanders among the attractor ruins close to the maximal gain mode at the tip of the ellipse shown in Fig. 2.4 (b) until a crisis occurs when the system gets too close to the antimodes on the upper branch. To generate these simulations, a noise amplitude of $R_{sp} = 1 \times 10^{-4}$ is added to the normalized Lang-Kobayashi equations to model realistic experimental conditions. This initiates a sudden shift in $\eta(t)$ and $n(t)$ to

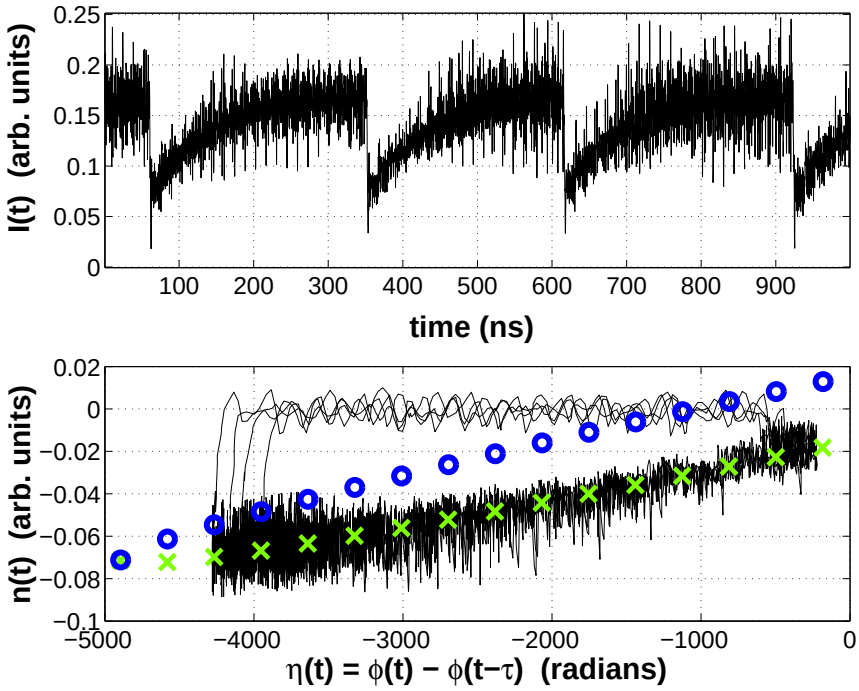

Figure 2.4: (a) Simulations of the LFF intensity dynamics and (b) the signature transitions between ECMs in the phase space of the external cavity phase shift $\eta(t)$ and carrier number $n(t)$ which typify this dynamical state. The crosses represent the ECMS while the antimodes are denoted by the circles on the upper half of the ellipse.

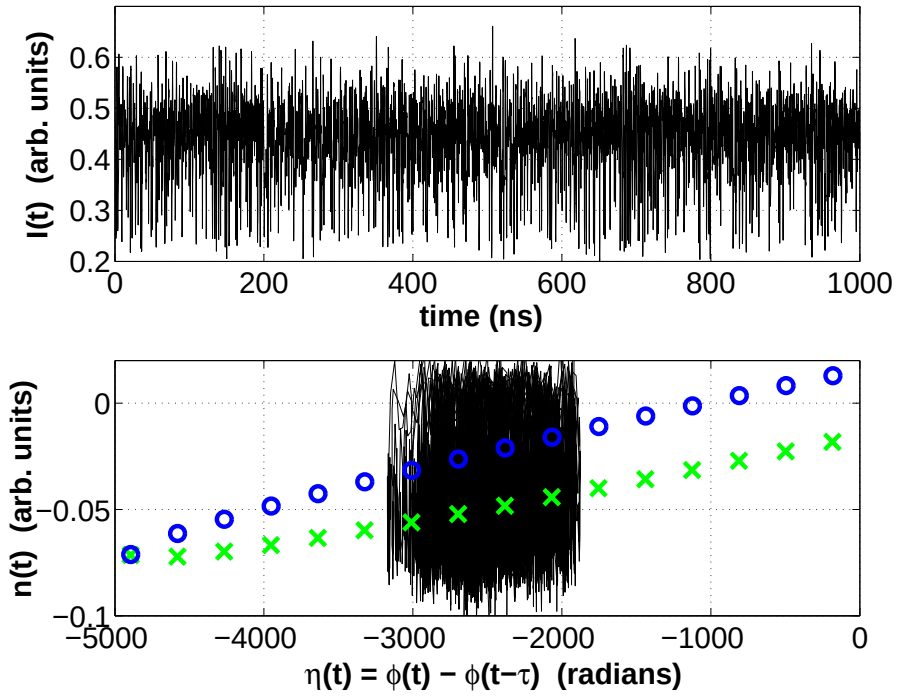

Figure 2.5: (a) The intensity dynamics of the CC regime demonstrate wild amplitude swings (b) are observed to localize around a smaller group of ECMs than the LFF state in the ($\eta(t)$,$n(t)$) representation. The crosses represent the ECMS while the antimodes are denoted by the circles on the upper half of the ellipse.

solitary lasing conditions, coincident with the dropout of intensity. A stepwise, itinerant recovery of the system variables towards maximum gain follows along the lower branch of the ellipse [51].

At larger injection currents, the system trajectory wanders more freely among the modes and antimodes throughout the ellipse, resulting in the signature large-amplitude fluctuations of the coherence collapse (CC) regime [50] shown in the intensity time trace in Fig. 2.5 (a). The phase space dynamics depicted in Fig. 2.5

(b) demonstrate that the CC dynamics are more tightly confined near the middle of the ellipse, and there is no overall push towards the maximum gain mode or long excursions on top of the antimodes towards solitary lasing conditions. The qualitatively different features measured in the light dynamics are clearly manifested in the allowed interactions observed to occur between the ECMs on the ellipse.

2.3 Experiment

The experimental setup utilized for all of the subsequent investigations is shown in Fig. 2.6. For each experiment, a Lincolnix LDC-201 temperature controller is used to stabilize (to better than 0.01K) a Fabry-Perot semiconductor laser with an antireflection coating of approximately 10% reflectivity on one facet and a high reflection coating on the other facet. Injection current is provided to the laser with a Newport Model 505 laser driver. The diverging light ($\lambda = 830\ nm$) emitting from the laser is collimated with a $\times 20$ microscope objective and reflected by a high-reflectivity ($\sim 98\%$) mirror. For each experiment a beam splitter directs light onto a New Focus Model 1181 photodetector (12 GHz bandwidth) for system diagnostics. The output of the photodetector is recorded using a Tektronix TDS7104 digital oscilloscope with 100 ps resolution.

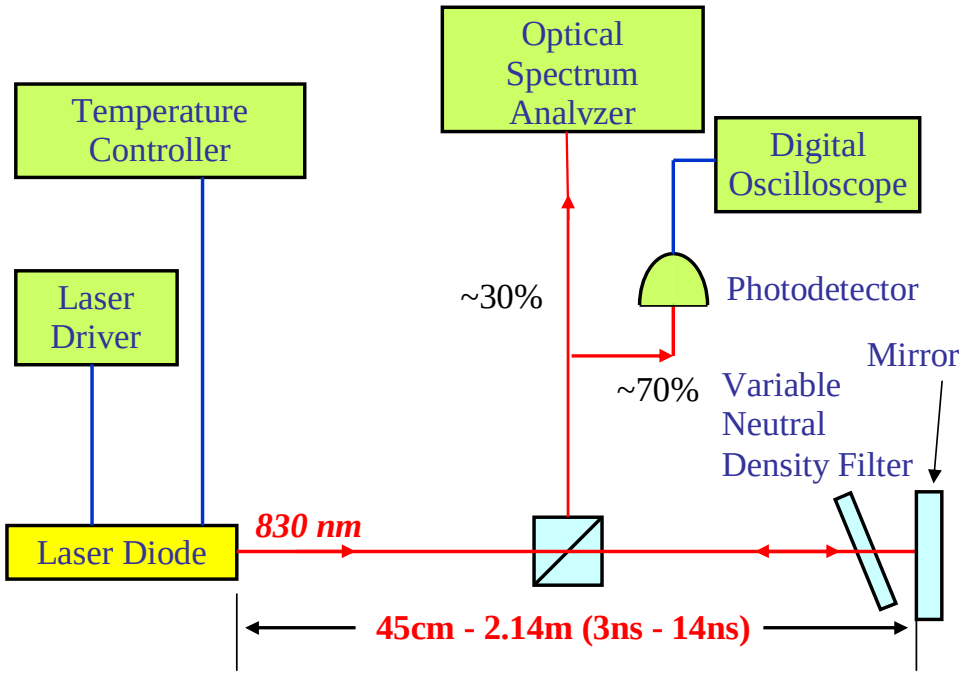

Figure 2.6: Experimental setup of semiconductor laser diode with external feedback from a mirror. The amount of feedback is adjusted using a variable neutral density filter.

Chapter 3

Hurst Exponent Measurements of Semiconductor Phase Dynamics

3.1 Overview

Time-delayed feedback has profound consequences on the dynamics of a semiconductor laser. However, as we saw with the low-frequency fluctuations (LFF) phenomenon at the end of the previous chapter, the deterministic scenerio predicted by the Lang-Kobayashi equations does not provide a complete picture of the dynamical instabilities which arise in the diode. Spontaneous emission must be additionally added to the model equations in order to shape the light output so that it resembles experimental observations. When deterministic and stochastic forces are both present in the system, can we discern the relative role that each term plays in driving the dynamics?

In this chapter, we address this question for the coherence collapse (CC) instability which arises at high injection currents in the laser. As opposed to the regular structures which appear in the power dropouts of the LFF state, the wild, chaotic oscillations of the intensity in the CC regime make it exceptionally difficult to distinguish the effect of spontaneous emission, and many numerical studies of this phenomenon neglect the contribution of noise [47]. Nevertheless, we find that the phase dynamics of the electric field betray the source which drives the fluctuations in the laser system. The relative contribution of deterministic and stochastic

influences may be quantitatively distinguished via Hurst exponent measurements of the optical phase fluctuations.

Quite often, it is possible to experimentally determine the amplitude of dynamical variables, but the measurement of phase variables is much more elusive. Gabor's [52] introduction of the Hilbert transform to define an analytic signal from the amplitude of a dynamical variable made it possible to derive an associated phase. In recent years, such phase variables have been important in the study of nonlinear oscillator dynamics and synchronization [53, 54]. When chaotic or noisy dynamics is displayed by such systems, the definition of a unique phase variable is often difficult due to the presence of multiple centers of rotation of the system trajectories.

In the context of the chaotic dynamics of the Lorentz model, Yalçinkaya and Lai [55] used an empirical mode decomposition method [56] and the Hilbert transform to provide a uniquely defined phase variable and examine its dynamics. They showed that the Hurst exponent for the phase dynamics of this model chaotic system was about 0.74, representing persistent fractional Brownian motion of the phase [32, 57].

We experimentally estimate the Hurst exponent for measurements made on a semiconductor laser with different levels of reflective feedback and compare these results with computations of the Lang-Kobayashi equations with additive Langevin noise [58]. Our results show that such measurements provide clear evidence for a transition from regular Brownian motion (stochastic driving) to persistent fractional Brownian motion (deterministic driving) of the phase as the amount of optical feedback coupled to the semiconductor laser is progressively increased.

3.2 Hurst Exponents

Random processes in biological and physical systems such as diffusion are often times described as a Brownian motion, where the trajectory of a measured variable may be described as a random walk. Specifically, the displacement of the variable at each time interval is determined by a Gaussian random process. However, in phenomenon such as *anomalous* diffusion, the deviations in the system at each time step are additionally influenced by previous motions undertaken by the system. In the 1950's Hurst developed an empirical scaling law to characterize long-range correlations he found in recordings of a variety of natural systems including river discharges, rainfall, and tree rings [32]. A decade later Mandelbrot put Hurst's observations in a more natural theoretical framework with the introduction of *fractional* Brownian motion as a generalization of the random process [33]. In this section we review Mandelbrot's definition of this phenomenon and show how measurements of the Hurst exponent reveal the degree of determinism (long-range correlations) in the evolution of a dynamical system.

3.2.1 Brownian Motion and Fractional Brownian Motion

Consider a time trace of a regular Brownian motion

$$B_r(t_i) = \sum_{j=1}^{i} G(t_j). \tag{3.1}$$

where the displacement at each time step is drawn from a Gaussian white noise source $G(t)$. The time trace displayed in Fig. 3.1 (a) represents a Brownian mo-

tion constructed from 100,000 increments of a Gaussian distribution possessing zero mean and a standard deviation of unity (arbitrary units). Although the overall displacement of the Brownian motion $\Delta B_r(w) = B_r(t_i) - B_r(t_{i'})$ does not deviate from zero over a time interval of $w = t_i - t_{i'}$ with $i > i'$, the variance of $\Delta B_r(w)$ increases linearly with w. Equivalently, the mean of the absolute value of $\Delta B_r(w)$ scales with w according to [59]

$$\langle |\Delta B_r(w)| \rangle \propto w^{\frac{1}{2}}. \tag{3.2}$$

where the angle brackets signify the average over many iterations of the process. To confirm this relationship for the time series in Fig. 3.1 (a), we slide a window with width w from the beginning to the end of the time series to calculate $\langle |\Delta B_r(w)| \rangle$. This quantity is computed for different w spanning many orders of magnitude. Finally, as shown in Fig. 3.1 (b), the logarithm of the average displacement is plotted against the logarithm of the window width. It is observed that the plot lies along a straight line with a slope of 0.49, confirming the scaling of the Brownian process.

Mandelbrot introduced the notion of fractional Brownian motion as a random walk where the individual increments at each time step depend on the whole history of previous displacements. In short, the random process present at each time step is weighted by a kernel of $(t_i - t_{i'})^{H-\frac{1}{2}}$ where the influence of the previous steps is characterized by the Hurst exponent H [33]. The fractional Brownian motion is defined then for a continuous time t as

$$B_H(t) = \frac{1}{\Gamma(H+\frac{1}{2})}\{\int_{-\infty}^{0}[(t-t')^{H-\frac{1}{2}} - (-t')^{H-\frac{1}{2}}]dB(t') + \int_{0}^{t}(t-t')^{H-\frac{1}{2}}dB(t')\}. \tag{3.3}$$

Long-range correlations are clearly present in this definition, and specifically, the

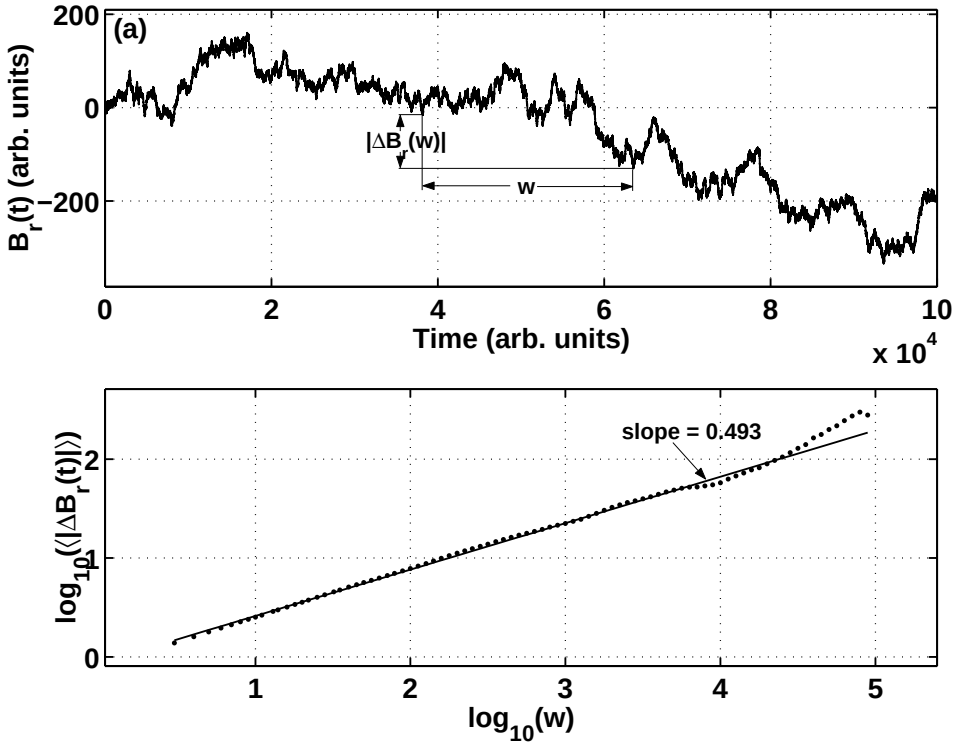

Figure 3.1: (a) a regular Brownian time trace built from 100,000 increments of a Gaussian noise source, (b) the logarithm of the mean absolute value $\langle|\Delta B_r(w)|\rangle$ is plotted against the logarithm of the window width w. A scaling of 0.49 is indicative that no correlation exists between the individual time increments.

Hurst exponent dictates the impact of future increments $B_H(t)$ with previous increments $-B_H(-t)$ via the correlation function [33]

$$C(t) = \frac{\langle -B_H(-t)B_H(t)\rangle}{\langle B_H(t)^2\rangle} = 2^{2H-1} - 1. \tag{3.4}$$

An approximation to a fractional Brownian motion may be numerically generated using successive random increments from Gaussian distribution and a finite memory. This motion is the summation [33]

$$B_H(t_i) = \sum_{k=1}^{i}[B_H(t_k) - B_H(t_{k-1})] \tag{3.5}$$

where the displacements are computed as

$$B_H(t_i) - B_H(t_{i-1}) = \frac{1}{\Gamma(H+\frac{1}{2})}[\sum_{j=i-M}^{i-2}((i-j)^{H-\frac{1}{2}} - (i-j-1)^{H-\frac{1}{2}})G(t_j) + G(t_{i-1})]. \tag{3.6}$$

The long-range correlations additionally affect the average absolute value of the displacements over an interval w. The scaling may now be typified as

$$\langle|\Delta B_H(w)|\rangle \propto w^H. \tag{3.7}$$

When $H = 0.5$, the kernel in Eqn. 3.3 and the correlation function [Eqn. 3.4] vanish over all time steps and the trajectory of the system may be described by a regular Brownian motion. However, for H values above or below 0.5, two distinct fractional Brownian motions may be discerned in the dynamics:

1. When $H < 0.5$ the correlation function is negative and the trajectory will tend to turn back upon itself. As a result, the overall fluctuations of the motion appear to be more constrained than a traditional Brownian motion and the system is said to exhibit *antipersistence*.

2. When $H > 0.5$ the correlation function is positive and the system demonstrates *persistence* in the dynamics. In this case an increasing (decreasing) trend in the past makes an increasing (decresing) trend in the future more probable.

The three panels in Fig. 3.2 display Brownian motions generated from Eqns. 3.5 and 3.6 with a Hurst exponent $H = 0.25$ [Fig. 3.2 (a)], $H = 0.50$ [Fig. 3.2 (b)], and $H = 0.75$ [Fig. 3.2 (c)]. To emphasize the effect of the scaling exponent, each time trace is built from the *same* sequence of random fluctuations (drawn from a Gaussian source) and utilizes a history length of $M = 10,000$ time steps. Although the overall motion in each panel is similar, the range of each vertical axis indicates the influence of previous deviations in the system. For instance, the antipersistant behavior in Fig. 3.2 (a) covers a smaller range than the regular Brownian motion in Fig. 3.2 (b). In contrast, the span of the vertical axis is drastically increased for the persistent motion in Fig. 3.2 (c).

3.2.2 Example: Stochastic and Deterministic Mode-Hopping

The LFF and CC instabilities exhibit markedly different features in the light output, yet, as revealed in the previous chapter, the two dynamical states share a common backbone of external cavity modes. The resulting light dynamics are therefore dependent on the *transitions* which occur between the lasing modes. Recall that for a sufficient amount of feedback, the external cavity modes lose their stability and the trajectory will itinerate among the attractor ruins available to the system. However, stochastic influences additionally affect the mode-hopping characteristics

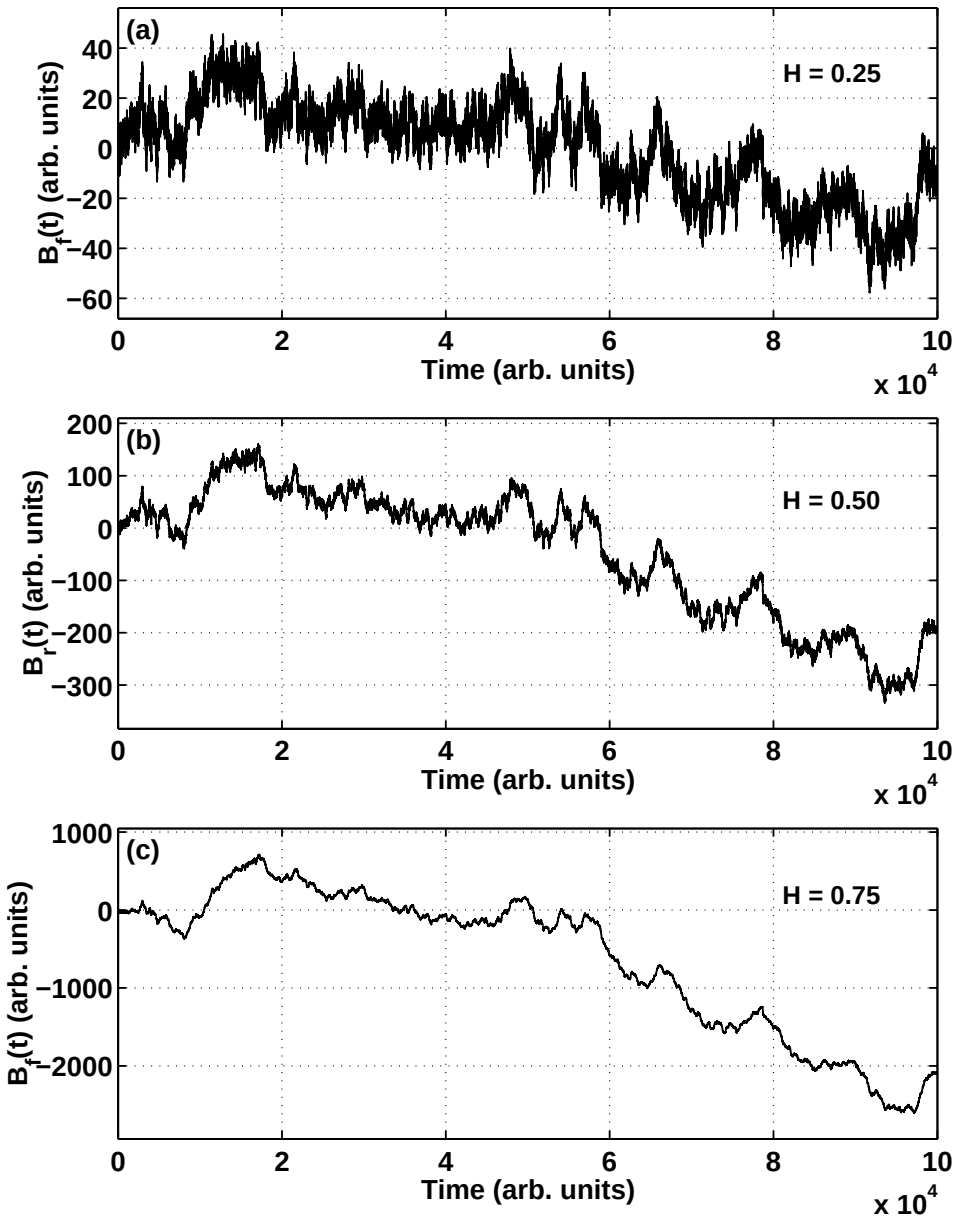

Figure 3.2: (a) anti-persistent fractional Brownian motion with Hurst Exponent of $H = 0.25$, (b) regular Brownian motion with Hurst Exponent of $H = 0.50$, and (c) persistent fractional Brownian motion with Hurst Exponent of $H = 0.75$. Each time series is computed from the same source of Gaussian fluctuations.

of the system. This may be concretely observed in Fig. 3.3 (a), where we integrate the model equations with Langevin noise at a low feedback level. An intensity time series is shown for a higher feedback strength in Fig. 3.3 (c).

When both deterministic and stochastic forces induce mode-hopping between the ECMs in the system, how may we determine the *dominant* influence in the transition dynamics? At this point it is instructive to look at the optical phase dynamics. In Fig. 3.4 (a) we plot the deviation of the phase about its average rate of rotation for the time traces in Fig. 3.3 (b) (thin line) at low feedback strength and at the higher feedback strength in Fig. 3.3 (d) (thick line). Note that we are now examining the raw (unwrapped) optical phase and not the external cavity phase shift previously considered. Each time series is sampled at 10 GHz in order to emphasize dynamical timescales which may be realized in an experimental setting. It is clear that the phase dynamics for the cases of deterministic and stochastic mode-hopping resemble a Brownian-like motion. The degree of determinism present in each motion may be estimated by calculating the Hurst exponent for each time trace.

In Fig. 3.4 (b) we plot logarithm of the mean absolute value of the phase displacement versus the logarithm of various window widths for each time series shown in Fig. 3.4 (a). The stars represent the phase displacements due to deterministic mode-hopping and the circles designate the motions due to noise-induced hops. In each case we find a scaling regime over about two decades of window width (from ~ 3 ns to ~ 20 ns). In this regime the dynamics are primarily dominated by inter-mode interactions as the inherent laser dynamics occur on much faster timescales (less than 1 ns). The stochastic-generated hopping between ECMs displays a regular

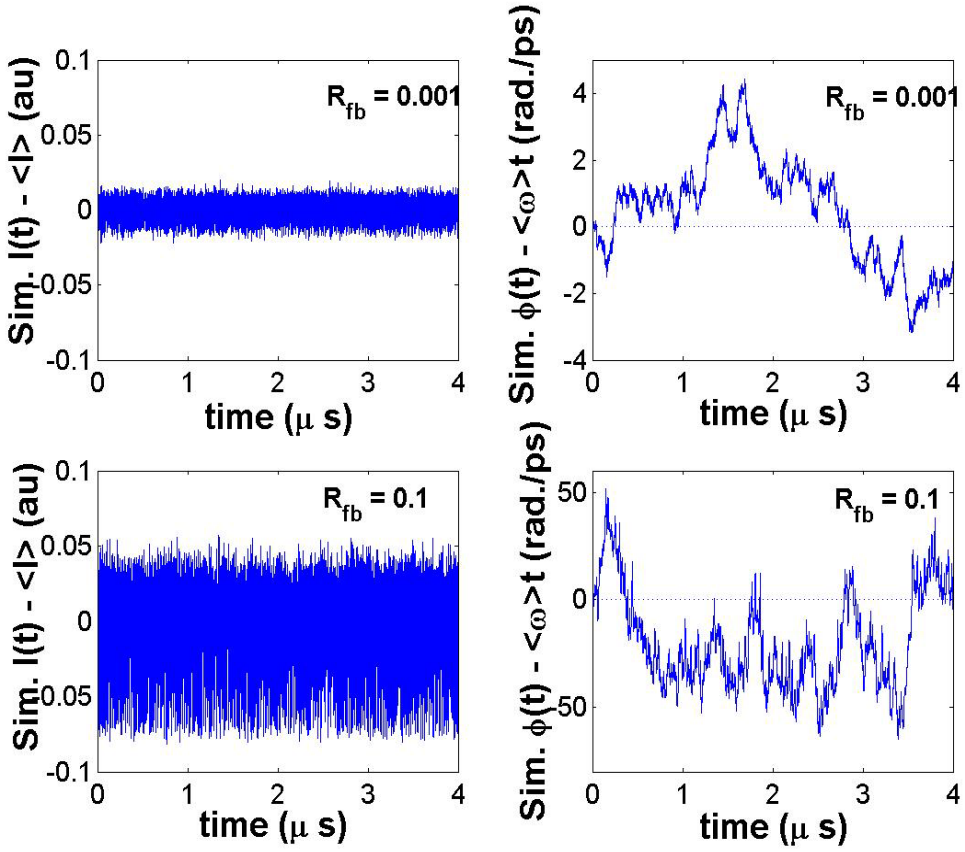

Figure 3.3: (a) Simulated intensity time series of the CC regime at a low feedback strength with a reflectivity of $R = 0.0001$, (b) optical phase fluctuations about the average phase increment for the time series in (a), (c) simulated intensity time series for the same parameters as (a) except for a higher feedback strength with a reflectivity of $R = 0.1$, and (d) optical phase fluctuations about the average phase increment for the time series in (c).

Brownian motion with a Hurst exponent $H = 0.52$ while the deterministic mode-hopping scales with $H = 0.74$, depicting a persistent fractional Brownian motion. The high value of the Hurst exponent in the latter case agrees wih our expectation that deterministic forces due to the delayed feedback produce long-range correlations in the time trace.

3.3 Hilbert Phase

The results of the previous section demonstrate that the optical field fluctuations contain relevant information about the influence of deterministic mechanisms in the laser system. The dynamics of the optical field phase are not easily detected in experimental situations, however, as the variations of the complex electric field occur at extremely fast timescales of $\sim 10^{12} - 10^{14}\ Hz$. Furthermore, intensity measurements of the light dynamics using a photodector destroys the optical phase content and oscilloscope time trace recordings are severly limited in bandwidth to 1 GHz. In the 1940's Gabor introduced the complex analytic signal as a method to extract phase information from a time series measurement of an amplitude variable [52]. The phase associated with the analytic signal has recently been utilized in nonlinear signal processing applications including chaotic oscillator dynamics [53, 60] and synchronization phenomenon [61]. Here we introduce the formulation of the analytic signal using the Hilbert Transform and point out the limitations of the physical significance of the derived phase information.

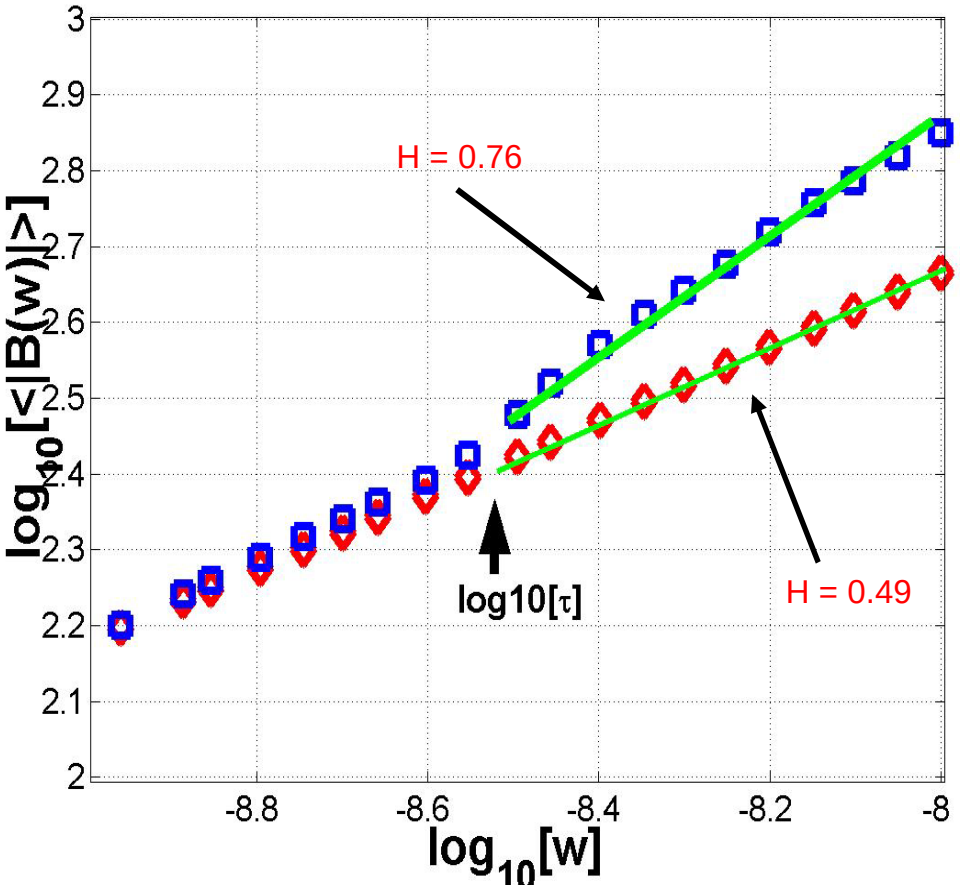

Figure 3.4: The mean absolute value of the phase displacement is measured at various window widths for the optical phase fluctuations depicted in Fig. 3.3 (b),(d) for respective feedback strengths of $R = 0.0001$ and $R = 0.1$. The scaling of the two optical phase fluctuations deviates for window widths larger than the external cavity round-trip time with an Hurst exponent estimate of $H = 0.49$ for $R = 0.0001$ and $H = 0.75$ for$R = 0.1$.

3.3.1 Definition

A complex analytic signal $I(t)$ may be constructed from a real time series $I^{(r)}(t)$ by defining an imaginary component $I^{(i)}(t)$ such that

$$I(t) = I^{(r)}(t) + iI^{(i)}(t). \tag{3.8}$$

The imaginary term must be defined carefully from $I^{(r)}(t)$ such that the amplitude and phase of the resultant analytic signal will exhibit a geometric rotation in the complex plane. Gabor recognized that this may be accomplished if the analytic signal possesses only the positive frequency content of the real signal, i.e.

$$I(t) = \frac{2}{\sqrt{2\pi}} \int_0^\infty a(\omega) e^{i\omega t} d\omega, \tag{3.9}$$

where

$$a(\omega) = \frac{1}{\sqrt{2\pi}} \int_{-\infty}^{\infty} I^{(r)}(t) e^{-i\omega t} dt \tag{3.10}$$

represents the Fourier transform of $I^{(r)}(t)$. After substituting Eqn. 3.3 into Eqn. 3.2 and separating the real and imaginary components, this analytic signal may be rewritten [62] as

$$I(t) = I^{(r)}(t) + i\frac{1}{\pi} PV \int_{-\infty}^{\infty} \frac{I^{(r)}(t')}{(t-t')} dt'. \tag{3.11}$$

The imaginary term

$$I^{(i)}(t) = i\frac{1}{\pi} PV \int_{-\infty}^{\infty} \frac{I^{(r)}(t')}{(t-t')} dt'. \tag{3.12}$$

is the Hilbert transform of $I^{(r)}(t)$ where PV represents the Cauchy principal value of the integral and $I^{(r)}(t)$ may be recovered from $I^{(i)}(t)$ by an additional Hilbert transform. It can furthermore be shown that the real (imaginary) component of

the analytic signal is the convolution of $\frac{1}{\pi t}$ and the imaginary (real) signal. Each component is highly sensitive to the instantaneous motions of the amplitude of its counterpart at each step in time.

The computation of the Hilbert transform is simplified by taking advantage of the spectral content of the analytic signal shown in Eqn. 3.9. In practice, the analytic signal may be built by (1) taking the Fourier transform of $I^{(r)}(t)$, (2) setting the negative frequencies to 0 and doubling the positive frequencies (so $I^{(r)}(t)$ contains the full $a(\omega)$), and (3) taking the inverse Fourier transform achieve $I(t)$. The imaginary component of $I(t)$ resulting from the inverse Fourier transform is the Hilbert transform of $I^{(r)}(t)$.

To analyze the rotations of the system in the complex plane, the analytic signal may be rewritten as

$$I(t) = A_H(t)e^{i\phi_H(t)}, \tag{3.13}$$

where the Hilbert amplitude $A_H(t)$ and Hilbert phase $\phi_H(t)$ are real functions of time. The instantaneous Hilbert frequency

$$\omega_H(t) = \frac{d\phi_H(t)}{dt}, \tag{3.14}$$

can always be calculated from the Hilbert phase. This frequency quantifies the rate of rotation of $I(t)$ in the complex plane.

3.3.2 Example

In Fig. 3.5 we demonstrate a calculation of the Hilbert phase from a short 6 *ns* segment of an experimental intensity time trace measured in the coherence collapse

regime. The real time series and its imaginary counterpart are shown in Fig. 3.5 (a). The Hilbert transform constructs $I^{(i)}(t)$ (grey line) such that it resembles $I^{(r)}(t)$ (black line) except with a phase lag of $\pi/2$. The trajectory of the analytic signal in the full complex plane is plotted in Fig. 3.5 (b). The phase lag of the imaginary component is manifested as rotational motions of the analytic signal around the mean amplitude of the time series (the origin in the complex plane). The full evolution of the Hilbert phase is displayed in Fig. 3.5 (c) without regard to jumps from 2π to 0. It is necessary for $\phi_H(t)$ to be unwrapped to deduce long range fluctuations of the Hilbert phase in Hurst exponent calculations.

Although there is a clear notion of geometric rotation for the analytic signal in the complex plane, in Fig. 3.5 (d) the instantaneous Hilbert frequency demonstrates negative values at the center of the time trace. The interval over which $\omega_H(t)$ dips to negative values is problematic since we are ascribing a physical significance to the Hilbert phase. The unphysical interval corresponds to a kink in the Hilbert phase time trace detailed in the inset of Fig. 3.5 (c). This kink is formed when the trajectory of the analytic signal revolves around a point away from the origin. This alternative point of revolution is denoted by the star in Fig. 3.5 (b). The loop made by $I(t)$ around this alternative reference level indicates that *multiple* centers of rotation exist in the complex plane of the analytic signal and the mean value of the amplitude does not sufficiently capture all rotations present in $I^{(r)}(t)$.

The above example shows that the instantaneous Hilbert frequency bears a physical interpretation only when the rotations in the complex plane take place around a single reference point. In the next section we explore the conditions a real

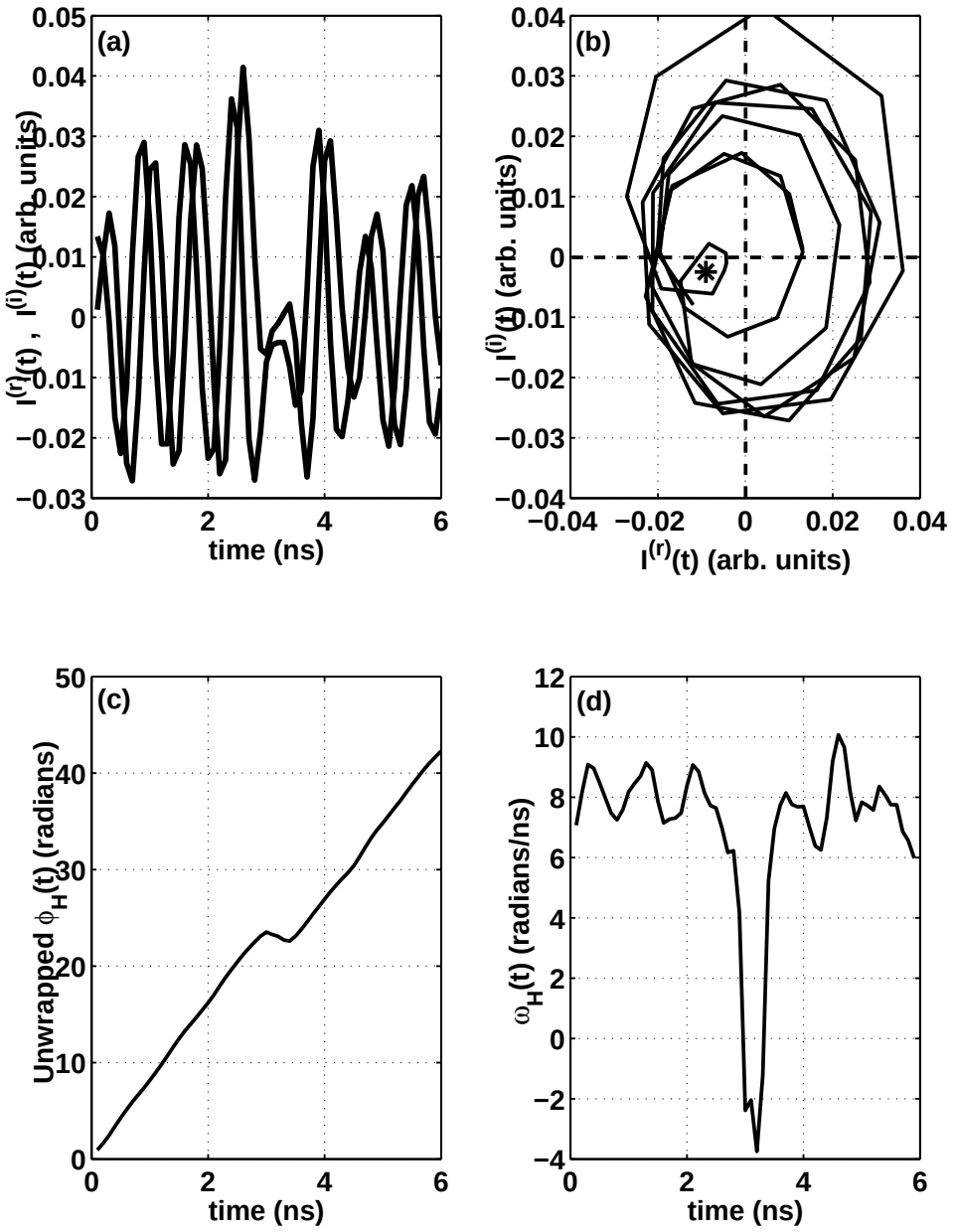

Figure 3.5: (a) the real (black line) and imaginary (gray line) components of the complex analytic signal (b) the full rotation of the trajectory in the complex plane, (c) the unwrapped Hilbert phase from the rotation, and (d) the instantaneous Hilbert frequency calculated from the Hilbert phase in (c). The unphysical negative interval of instantaneous Hilbert frequencies is associated with rotations centered around the star in (b) and corresponds to the kink in (c).

signal must satisfy to achieve a proper sense of rotation. A novel technique [56, 63] is then introduced to empirically decompose an arbitrary real signal into components which individually yield a physically significant Hilbert phase.

3.4 Empirical Mode Decomposition

The Hilbert phase analysis in the last section measured the rotations of the analytic signal about the mean value of an intensity time series. While this is an intuitive and preferred reference level for gauging the fluctuations of an amplitude variable, it is certainly not a *unique* choice. For instance, the time interval of the instantaneous Hilbert frequency displaying negative values in Fig. 3.5 (d) would show physically relevant values if the Hilbert phase analysis was instead centered at the red star in the complex plane in Fig. 3.5 (b). An unambiguous Hilbert phase may only be defined if the system exhibits *proper rotation*; namely, there is a preferred direction of rotation for $I(t)$ in the complex plane which can be defined with respect to a unique center. These conditions ensure that the instantaneous Hilbert frequency does not reflect fluctuations of the amplitude induced by asymmetric waveforms [56].

Many nonlinear oscillators, however, will display multiple centers of rotation in the complex plane. A nonstationary time series will certainly exhibit multiple reference levels of fluctuation, but this phenomenon is more commonly caused by the simultaneous presence of disparate frequencies in the real signal. In this case, the reference level of a high-frequency oscillation in the system is modulated by the lower-frequency components and a static level is irrelevant for typifying the Hilbert

phase of the system. This explains why Hilbert phase analysis has mainly been utilized in systems with one dominant frequency component such as the Rössler attractor [53] or in situations where the signal has been band-pass filtered to a narrow frequency range [61].

3.4.1 Intrinsic Mode Functions

When multiple timescales are present in a signal, the only way to make sense of amplitude fluctuations is to separately consider the oscillations comprising the system. In the past decade Nordon Huang has introduced the Empirical Mode Decomposition (EMD) method to adaptively separate an arbitrary real time series into components, each possessing a proper rotation structure, according to the innate time scales of the dynamics [56]. The signal is then expressed as a sum of intrinsic mode functions (IMF) which satisfy the following two conditions:

1. In the whole data set, the number of extrema and the number of zero-crossings must either equal or differ at most by one.

2. At any point, the mean value of the envelope defined by the local maxima and the envelope defined by the local minima is zero.

The EMD process is summarized as follows:

1. Construct two smooth splines connecting all the maxima and minima, respectively, to get $I^{(r)}_{max}(t)$ and $I^{(r)}_{min}(t)$.

2. Compute $\Delta I^{(r)}(t) \equiv I^{(r)}(t) - [I^{(r)}_{max}(t) + I^{(r)}_{min}(t)]/2$.

3. Iterate steps 1 and 2 for $\Delta I^{(r)}(t)$ until the resulting signal corresponds to a proper rotation. Denote the resulting signal by $C_1(t)$, which is the first intrinsic mode.

4. Take the difference $I_1^{(r)}(t) \equiv I^{(r)}(t) - C_1(t)$ and repeat step 1 to 3 to obtain the second intrinsic mode $C_2(t)$.

5. Continue the procedure, known as sifting, until the mode $C_M(t)$ shows no apparent variation.

By doing these steps, we have decomposed the original signal $I^{(r)}(t)$ into $\sum_{j=1}^{M} C_j(t)$, where each $C_j(t)$ generates a proper rotation in the complex plane. The $\Delta I^{(r)}(t)$ produced in step two picks out the highest frequencies present in the system by removing the modulation of the reference level by the low-frequency content of the signal. This high-frequency component is subtracted from the original time series once it satisfies the conditions of an IMF within a given tolerance [64]. The remaining modes highlight slower and slower timescales in the system until only a residual trend (without any oscillation) remains. In systems with a broad spectrum, the number of zero-crossings in successive IMFs roughly decreases by a factor of two. As a result, the EMD procedure has been compared with the hierarchical structure of a filter bank observed in wavelet decompositions [65].

In Fig. 3.6 the EMD is applied to the real time series considered in Fig. 3.5. Note that only 4 IMFs [Fig. 3.6 (a)-(d)] result from the fluctuations of $I^{(r)}(t)$ shown in Fig. 3.5 (a) where the final IMF represents the residual trend in the system. We next apply the Hilbert phase analysis to each IMF generated in the process. The

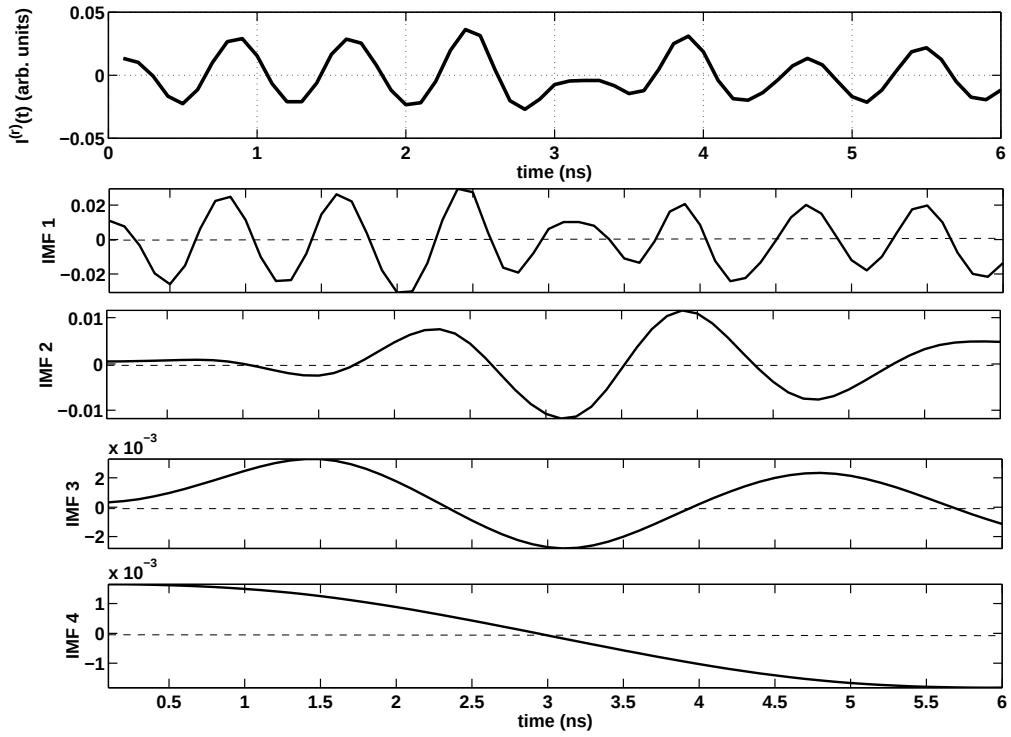

Figure 3.6: Four intrinsic mode functions (IMF) (a)-(d) are generated using the EMD method on the real time series shown in Fig. 3.5 (a). The sifting procedure guarentees that each IMF exhibits proper rotation.

trajectory of each analytic signal in the complex plane is respectively plotted in Fig. 3.7 (a)-(c). Here a common center of rotation is apparent for each IMF and an unambiguous Hilbert phase may be defined at each timescale. The corresponding instantaneous Hilbert frequency of each mode [Fig. 3.7 (d)-(f)] only takes positive values, thereby retaining a physical sense of rotation throughout the entire time series. The fluctuations of $I^{(r)}(t)$ are completely described then by the set of Hilbert phases generated by the constituent IMFs.

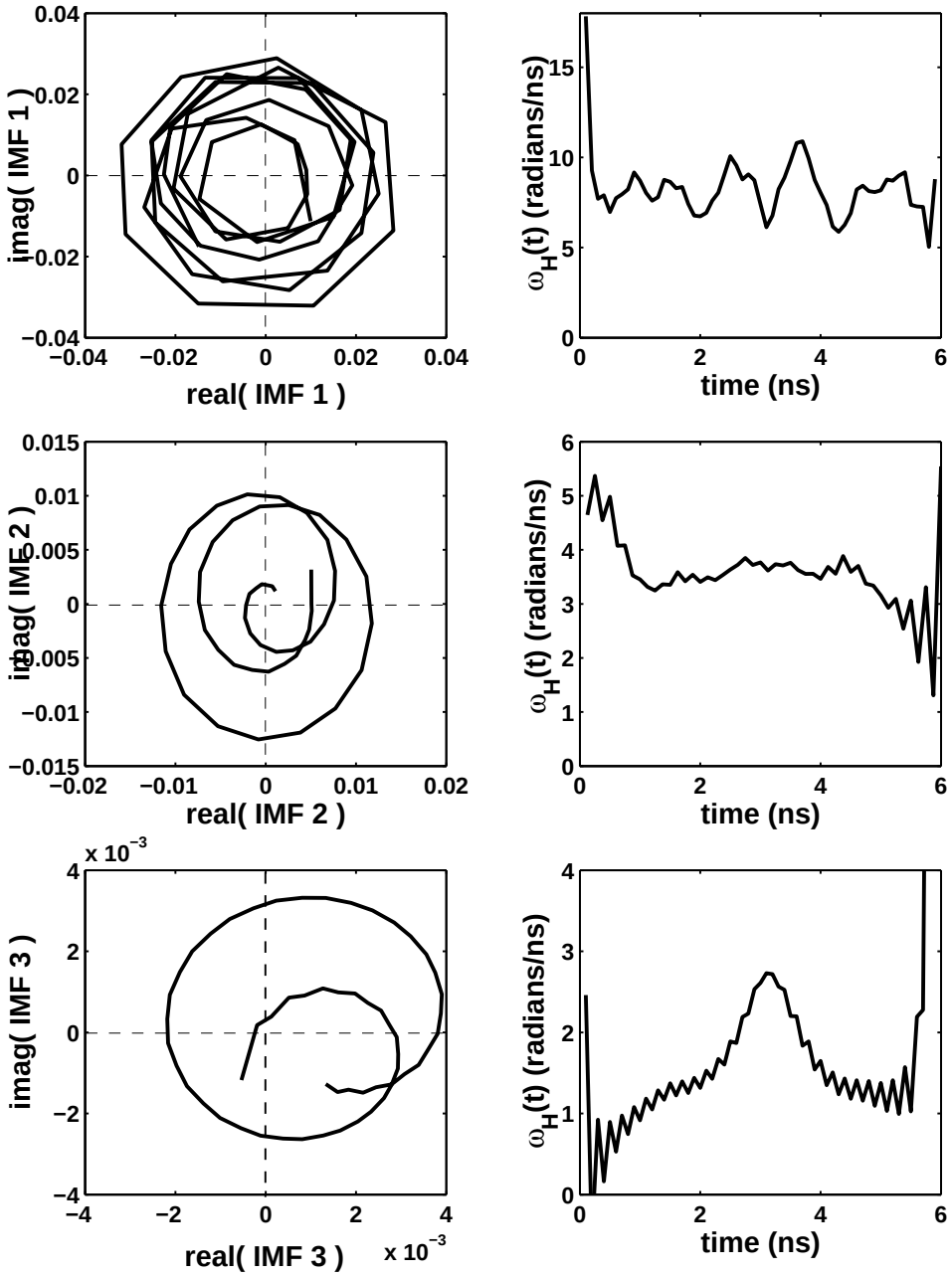

Figure 3.7: In (a)-(c) the trajectory of analytic signal from the fist three intrinsic mode functions (IMF) in Fig. 3.6 (a)-(c) shows a unique center of rotation. The corresponding instantaneous Hilbert frequencies in (d)-(f) demonstrate positive frequencies throughout the evolution of the time series.

3.5 The Transition to Fractional Brownian Motion

The techniques developed in the previous two sections allow us to derive a physically significant Hilbert phase from an intensity time series. We consider the experimental setup shown in Fig. 2.6 using a Sharp LT015MD laser diode and an external cavity round-trip time of 3 ns. The system is pumped at a bias current level of 71.6 mA which is 1.25 times the threshold current of 57.2 mA. For the experimental time series shown in Fig. 3.8 (a) with a feedback strength of $R = 6.7 \times 10^{-2}$ (here R is the reflectivity found in Eqns. 2.18), the EMD generates 14 IMFs, shown from Fig. 3.8 (b) to 3.8 (o). The properties of the IMFs ensure a proper structure of rotation for the corresponding analytic signals.

In Fig. 3.9 (a) the 14 Hilbert phases and the corresponding uniform phase increments calculated by $\langle \omega_{Hi}(t) \rangle t$ are plotted. Here $omega_{Hi}(t)$ is the instantaneous Hilbert frequency defined in Eqn. 3.14. The Hilbert phases (solid line) fluctuate about the dashed line representing the uniform phase increment. This is more clearly shown in Fig. 3.9 (b), where $\delta\phi_{H1}(t) = [\phi_{H1}(t) - \langle \omega_{H1}(t) \rangle t]$ is portrayed for the intensity time series of Fig. 3.8 (a) (thin line). We have focused on ϕ_{H1} since this phase variable represents the fastest observed time scales for the laser system. The 10 GHz sampling of the laser intensity enables us to observe the scaling of the phase fluctuations on the time scales of the dynamical interactions between external cavity modes. The phase fluctuations of the first IMF is also shown for a time series recorded for a weaker feedback strength of $R = 7.2 \times 10^{-4}$ (thick line).

To examine the nature of the phase fluctuations, in Fig. 3.9 (c) we plot

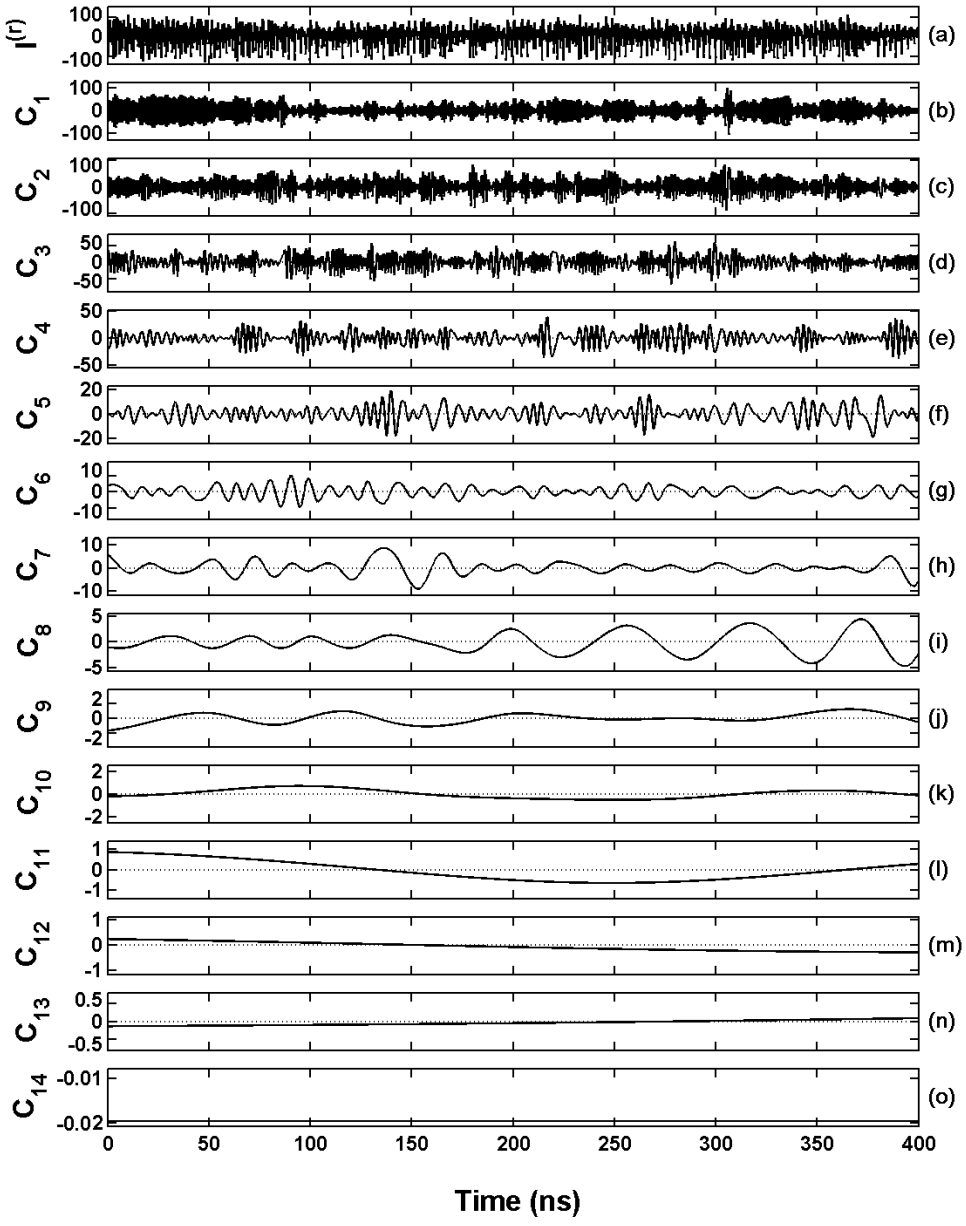

Figure 3.8: (a) Intensity output of the semiconductor laser with $I = 71.6\ mA$ and $R = 6.7 \times 10^{-2}$, (b)-(o) 14 intrinsic mode functions for the time series of (a).

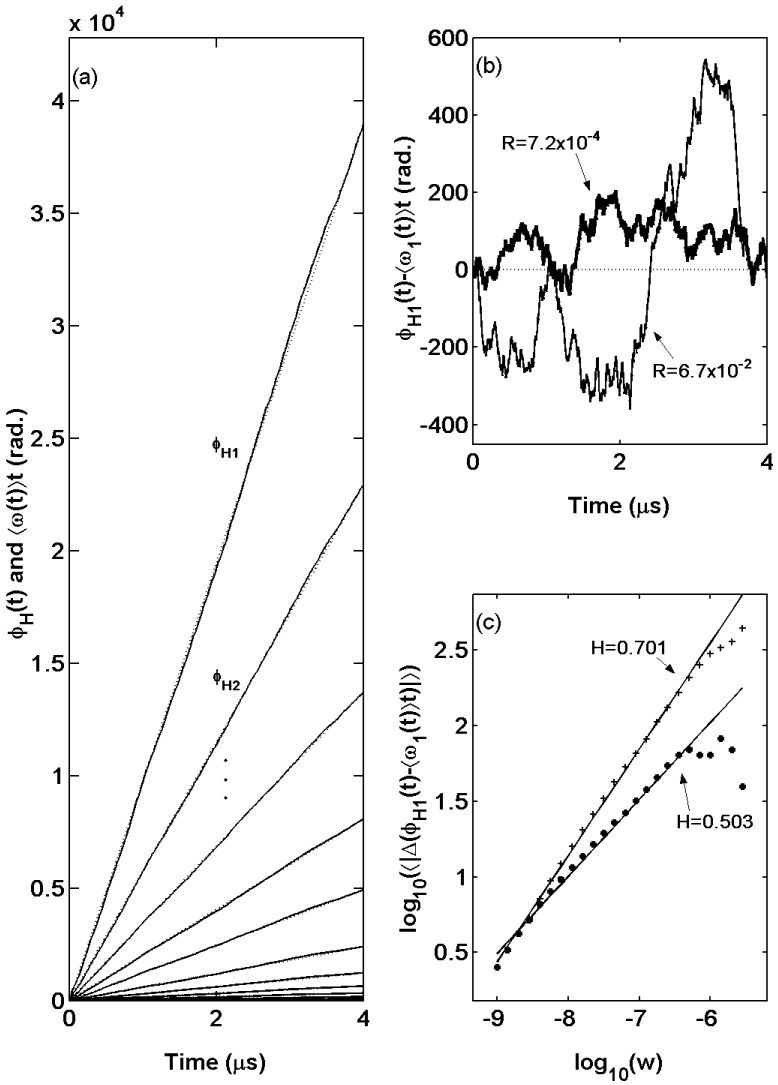

Figure 3.9: (a) The Hilbert phases $\phi_{Hi}(t)$ of the IMFs in Fig. 3.8 (solid line) and the corresponding uniform phase increment $\langle\omega_i(t)\rangle t$ (dashed line), where $i = 1 \ldots 14$, (b)the fluctuation of $\phi_{H1}(t)$ about the uniform phase increment $\langle\omega_1(t)\rangle t$ for (a) (thin line) and for a time series (not shown) with feedback strength $R = 7.2 \times 10^{-4}$ (thick line), and (c) the Hilbert phase dynamics is a persistent fractional Brownian motion with $H = 0.71$ for $R = 6.7 \times 10^{-2}$ and regular Brownian motion with $H = 0.50$ for $R = 7.2 \times 10^{-4}$.

$\log_{10}(\langle|\Delta\phi_{H1}(t)|\rangle)$ versus $log_{10}w$ for the phase fluctuations shown in Fig. 3.9 (b). Similar to the optical phase fluctuations, we find that a well-defined scaling regime persists over about two decades of window width (from ~ 3 ns to ~ 150 ns). The Hilbert phase dynamics of the semiconductor laser with a feedback of $R = 7.2\times10^{-4}$ displays regular Brownian motion with a Hurst exponent $H = 0.50$. This is an indication that the fluctuations of the phase are dominated by spontaneous emission noise inherent to the laser diode. For a stronger feedback of $R = 6.7\times10^{-2}$, we measure $H = 0.71$. In this case, the dynamics portray a persistant fractional Brownian motion of the phase and the fluctuations are primarily influenced by the delayed feedback.

In order to obtain a clearer picture of how the phase dynamics are influenced by the feedback strength, we record 13 data sets with increasing feedback levels from $R = 0$ to $R = 0.18$, shown in Fig. 3.10 (a)-(m). Our measurements in this coherence collapse regime are characterized by rapid transitions between external cavity modes.

For the Hurst exponent analysis, we obtained eight intensity time traces for every feedback strength in the experiment. We could then calculate the average Hurst exponent and the standard deviation of the eight samples for each of the 13 feedback strengths. The results are displayed in Fig. 3.11 by the triangles. When the feedback strength changes from $R = 0$ to $R = 6.4\times10^{-3}$, the Hurst exponent stays close to 0.5 and the phase dynamics resemble regular Brownian motion. Spontaneous emission noise is the driving force of the intermode switching dynamics for this range of feedback and there are no long-range correlations present in the time series. If

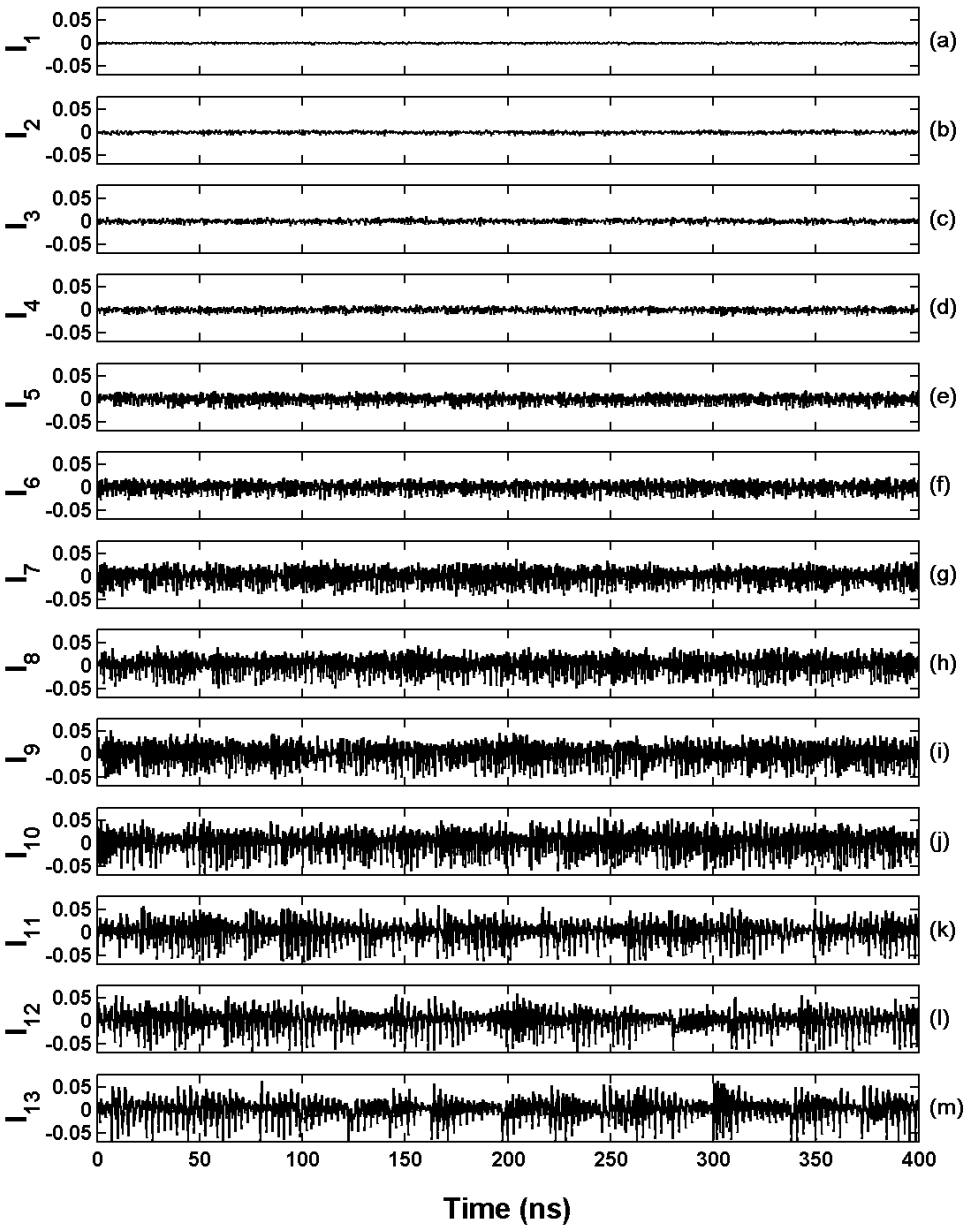

Figure 3.10: (a)-(m) Experimental intensity time series with increasing feedback strength from $R = 0$ to $R = 0.18$. The pump current is set at 71.6 mA.

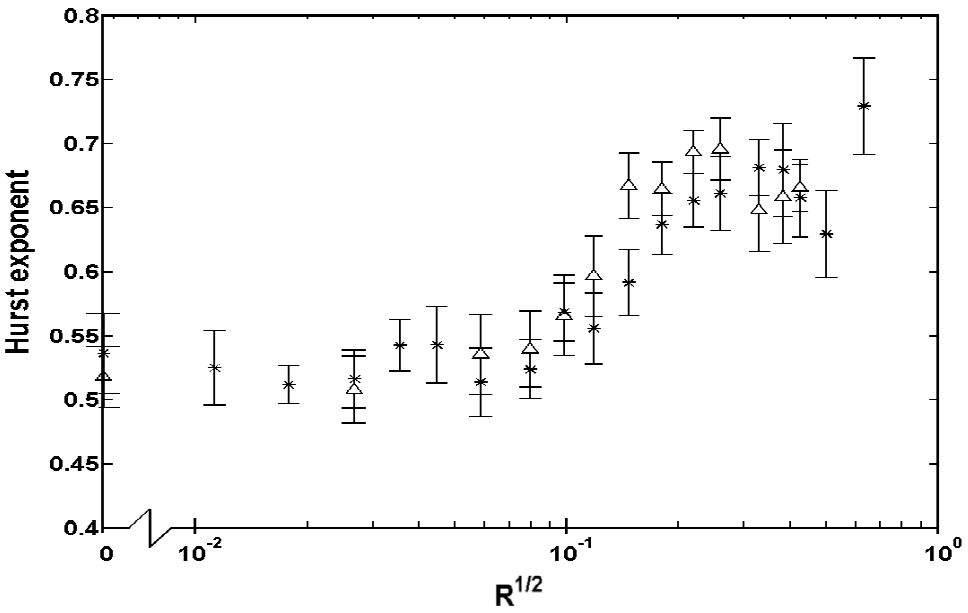

Figure 3.11: The Hurst exponent with error bars for experimental measurements (triangles) and simulations (stars) for different feedback strengths R shows the transition from regular ($H = 0.5$) to fractional ($H > 0.5$) Brownian motion. Each Hurst exponent is measured over a range of window widths from 3 ns to 150 ns.

the amount of feedback is increased past $R = 6.4 \times 10^{-3}$, the Hurst exponent exhibits a sharp increase towards 0.7 and levels off for feedback strengths greater than $R = 4.8 \times 10^{-2}$. In this regime, the phase dynamics is influenced by feedback and depends strongly on the history. Many external cavity modes now participate in the laser dynamics [66, 47], and the Hurst exponent we compute now reflects an average of the scaling behavior of the phase dynamics for individual modes as well as contributions from deterministic global intermode interactions.

The experiment may be numerically modeled by integrating the full Lang-Kobayashi Eqns. **??** and **??** with the following parameter values: $N_{th} = 3.9 \times 10^8$,

$\alpha = 5$, $G_{N,0} = 21400\ s^{-1}$, $r_0 = 0.32$, $r = 0.1$, $\tau = 3.0\ ns$, $R_{sp} = 10^{14}\ s^{-1}$, $\tau_r = 1.1\ ns$, $\Gamma = 1.1\ ps^{-1}$, $\tau_{in} = 3.9\ ps$, and $P_I = 1.25$. The equations are integrated with a time step of 0.5 ps for 41 μs (we neglect the first 1 μs for transients), low pass filtered and smoothed over intervals of 0.1 ns to simulate the digital oscilloscope electronics.

In Fig. 3.11 we also report the Hurst exponent versus the reflectivity from the simulations (stars), calculated for different effective external mirror reflectivity R values matching the experiment and some additional cases. The computational results support the experimental conclusion that the dynamics of the Hilbert phase display ordinary Brownian motion for feedback strengths up to $R = 6.4 \times 10^{-3}$. Further increases in feedback show a transition to fractional Brownian motion and saturation of the Hurst exponent to $H \sim 0.7$, displaying a close match with experimental measurements.

3.6 Conclusion

We have experimentally confirmed for a real system the prediction of Yalçhinkaya and Lai [55] of persistant Brownian motion for the most rapidly varying phase associated with a model chaotic system. In addition, we demonstrate that it is possible to distinguish between the influence of spontaneous emission noise and deterministic feedback on the dynamics of a semiconductor laser with optical feedback. The laser makes a transition from regular Brownian motion to persistant fractional Brownian motion as the external mirror reflectivity is increased. The occurence of this transition is quantified by measurements of the Hurst exponent for the phase dynamics

computed from the experimental and numerical intensity time series of the laser system.

Chapter 4

Chaotic Itinerancy in the Light and Carrier Dynamics

Near lasing threshold, spontaneous emission is such a prevalent force that many studies have questioned whether nonlinear dynamical processes resulting from reflective feedback are relevant for the description of the observed phenomena. Identification of chaotic itinerancy is especially difficult in experiments, where typically only one scalar variable may be measured directly. Streak camera measurements of the light dynamics on very short time scales have provided indirect confirmation of the deterministic scenario of low-frequency fluctuations (LFF) predicted from the Lang-Kobayashi equations [67]. Hilbert phase information extracted from filtered intensity measurements has previously demonstrated external cavity mode shifts [60].

In this chapter, we are interested in characterizing the itinerant motions displayed in *simultaneous measurements of the light and carrier dynamics* during the course of a dropout event. In order to elicit features common to many individual dropouts, we form a statistical description of the process from a large number of dropouts by calculating the experimental prehistory and posthistory probability distribution functions [34] for the intensity and voltage fluctuations across the laser diode. Optimal paths extracted from the probability distributions serve as building blocks to reconstruct the phase space dynamics of the dropout event. The

resulting trajectory highlights episodic transitions between low-dimensional attractor ruins [24] and demonstrates excellent agreement with simulations of the intensity and carrier number.

4.1 The Prehistory Probability Distribution Function

As dropouts in the light dynamics are problematic for many applications involving semiconductor lasers, the origin of this nuisance has been a subject of avid interest for the past three decades. Since the LFF phenomenon is primarily observed in experiments at low injection currents near the solitary lasing threshold, many studies have focused on the role that spontaneous emission noise plays in shaping this instability. A nonlinear stability analysis performed by Henry and Kazarinov reduced the infinite-dimensional Lang-Kobayashi equations to an approximate one-dimensional equation of motion for the carrier number in a potential well [48]. The analysis only considered small fluctuations in the intensity and phase about the maximum gain mode due to stochastic influences. In this context power dropouts are seen as escapes from the maximum gain mode over a potential barrier. Despite the simplicity of this model, experiments have verified that this potential formulation accurately captures the dependence of the dropout rate on the injection current and feedback level [68]. Over the parameter regime where this model is applicable, then, it is therefore desirable to experimentally discern features of the potential barrier in order to gain further insight into the process of noise-induced escape.

Large fluctuations appear in a variety of non-equilibrium systems including

switching in multistable lasers, Josephson junctions [70], protein folding, and electronic circuits [69]. In many of these systems, the large fluctuation is the result of noise-induced escape from a metastable state. A remarkable feature in many of these systems is that the exit path of escape to the extreme state often lies along a narrow tube of trajectories [71]. The probability that the escape occurs within this tube is exponentially larger then all other paths. The prehistory probability distribution function has recently been introduced as a tool that experimentally uncovers the distribution of trajectories which escape from a metastable state. This distribution evaluates the density of paths which pass through a coordinate of the phase space at each time step preceding the extreme event. The prehistory distribution generally displays a distinct peak, known as the optimal path, indicating how the system is most likely to move.

The first experimental application of this technique analyzed the fluctuations leading to dropout events in a semiconductor laser with external optical feedback. In Fig. 4.1 we reproduce the prehistory distributions measured by Hales et al. [35] for the intensity dynamics of 1512 dropout events (bottom) and a model of activated escape over a potential barrier (top). The dropout trajectories are aligned at the moment of escape ($t = 0$), defined in this case to be the point where the intensity is 10% above the extreme dropout level. The experiment was conducted near solitary lasing threshold with a high feedback strength and a delay cavity round trip time of 3 ns. The intensity data was recorded with a 125 MHz bandwidth photodetector and digitized with a sample period of 1 ns.

Even with this limited resolution the prehistory distribution of the LFF phe-

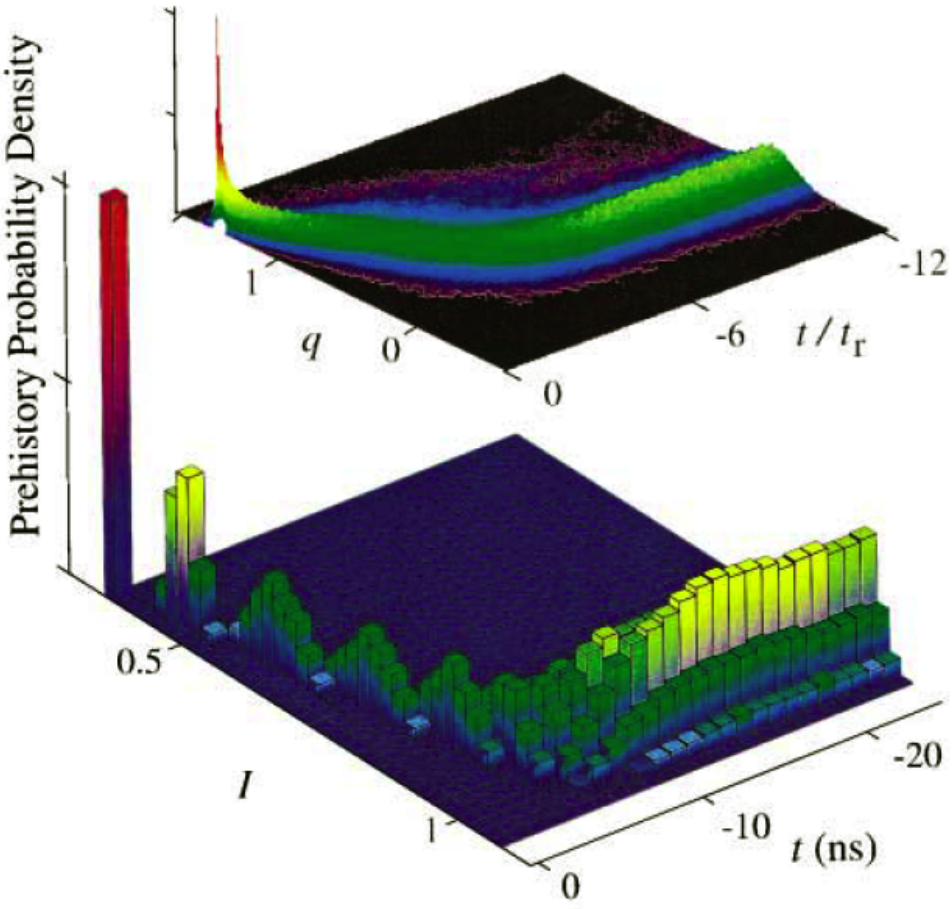

Figure 4.1: The prehistory probability distribution function for two manifestations of activated escape from a potential barrier (top distribution) and an experimental distribution constructed from many dropout events in a semiconductor laser.

nomenon demonstrates a well- defined peak at the moments immediately preceding the extreme event as well as for times far from the event ($t < -10\ ns$). However, there is a characteristic broadening of the distribution in the intermediate time interval ($-3\ ns < t < -10\ ns$). The distribution for the activated escape model more or less portrays a similar broadening phenomenon. The sharp peaks in each distribution correspond to motions of the system near the bottom of the potential well (for t far from the dropout) and across the potential barrier (right before the moment of dropout). The prehistory distribution becomes wider when the trajectory lies near the top of the potential barrier which is flatter and therefore more sensitive to fluctuations of the noise.

4.2 LFF as a Chaotic Itinerancy

The Lang-Kobayashi equations have been very successful in describing the dynamical behavior of power dropouts, motivating countless investigations of the deterministic phenomenon. Sano originally characterized LFF as a chaotic itinerancy with a drift [51]. In this interpretation, the dropout pulse occurs as the result of a crisis when the trajectory of the system wanders too close to the antimodes near the maximum gain mode, initiating a sudden shift in the system variables to solitary lasing conditions. The system then drifts across hundreds of external cavity modes (for moderate feedback strengths) towards the maximum gain mode supported by the feedback system. Shortly after this picture of the laser dynamics was formulated, an analytical consideration of the Lang-Kobayashi equations predicted that

itinerant motions between the external cavity modes is manifested in the unfiltered intensity as a series of pulses with a short duration of $50 - 200\ ps$. These pulses were soon experimentally confirmed through streak camera measurements of the light dynamics on short time scales.

A numerical realization of these rapid intensity pulses is shown in Fig. 4.2 (a). However, when these pulses are bandwidth limited in oscilloscope recordings ($1GHz$), the dynamics of the recovery resemble the staircase structure plotted in Fig. 4.2 (b). After the initial drop towards zero emission, the intensity levels out and iteratively grows along a series of steps towards the maximum gain mode. The amount of time spent in each step corresponds to the round trip time of the light in the external cavity. This manifestation of the itinerancy becomes apparent when we plot the *unfiltered* trajectory of the carrier number in Fig. 4.2 (c). The staircase structure arises due to the slow time scale of the carrier fluctuations ($\sim\ GHz$).

Each dropout pulse evolves in a similar manner, and characteristics of the dropout process may be deduced statistically. Hegarty found that many dropouts exhibit damped relaxation oscillations immediately after the initial fall of the intensity [72]. The stair structure in the recovery of the intensity has been extensively studied by Liu et al. [73]. Their findings suggest that the laser is 'locked' near a particular compound cavity mode in each step of the recovery. The sequence of steps is associated with an ordered sequence of external cavity modes and occurs for each dropout in a time series.

In the next few sections we repeat the experiment of Hales et al. with higher resolution equipment and show that the prehistory distribution reveals deterministic

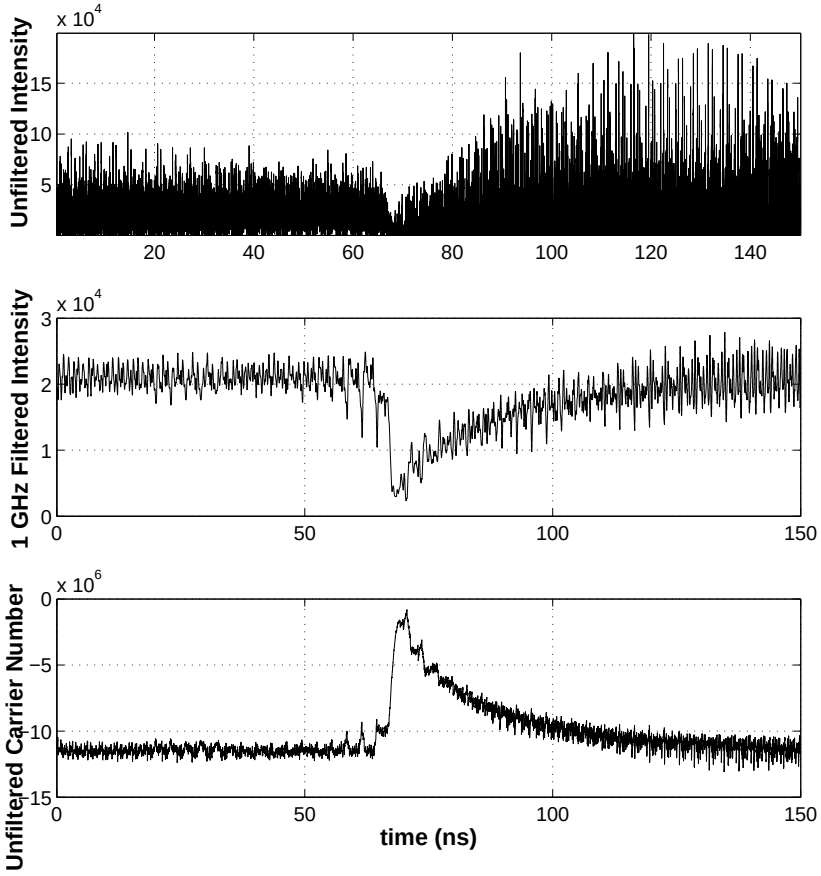

Figure 4.2: (a) The short pulses of a simulated time trace of a dropout event. (b) The filtered intensity demonstrates a stair structure recovery of the light dynamics as a result of the slow dynamics observed in (c) the unfiltered carrier density.

characteristics in the system *before* the dropout at the time scale of the external cavity round trip time. We additionally introduce the posthistory distribution to evaluate itinerant characteristics of the light dynamics in the recovery process towards maximum gain. The dropout dynamics of the population inversion are considered in measurements of the diode voltage fluctuations during the extreme event.

4.3 Experiment

For the experiment we set the injection current of the diode (RLT8340G) to 48.7 mA, which is 1.01 times the injection current, and subject the diode to a feedback that reduces the threshold current by about 10%. Concurrent measurements of the intensity from the photodetector and the voltage fluctuations across the laser diode indicate that the diode voltage exhibits pulsations when the intensity has power dropouts—they occur *simultaneously*, an observation [74] first made only a few years after the discovery of LFF [75].

These voltage fluctuations represent changes in the current (carrier number) across the laser diode. The time scales of the LFF are too fast to be controlled by the laser power supply, and so the diode voltage fluctuations are a good representation of the population inversion dynamics. We note that a 24 ns oscillation inherent to the electronic loop involved in voltage detection is present independent of the external cavity delay time. The effect of the electronics is deconvoluted by passing the measured voltage through a notch filter RLC circuit. The electronics loop consists of a parallel measurement of the laser diode and laser power supply through a BNC

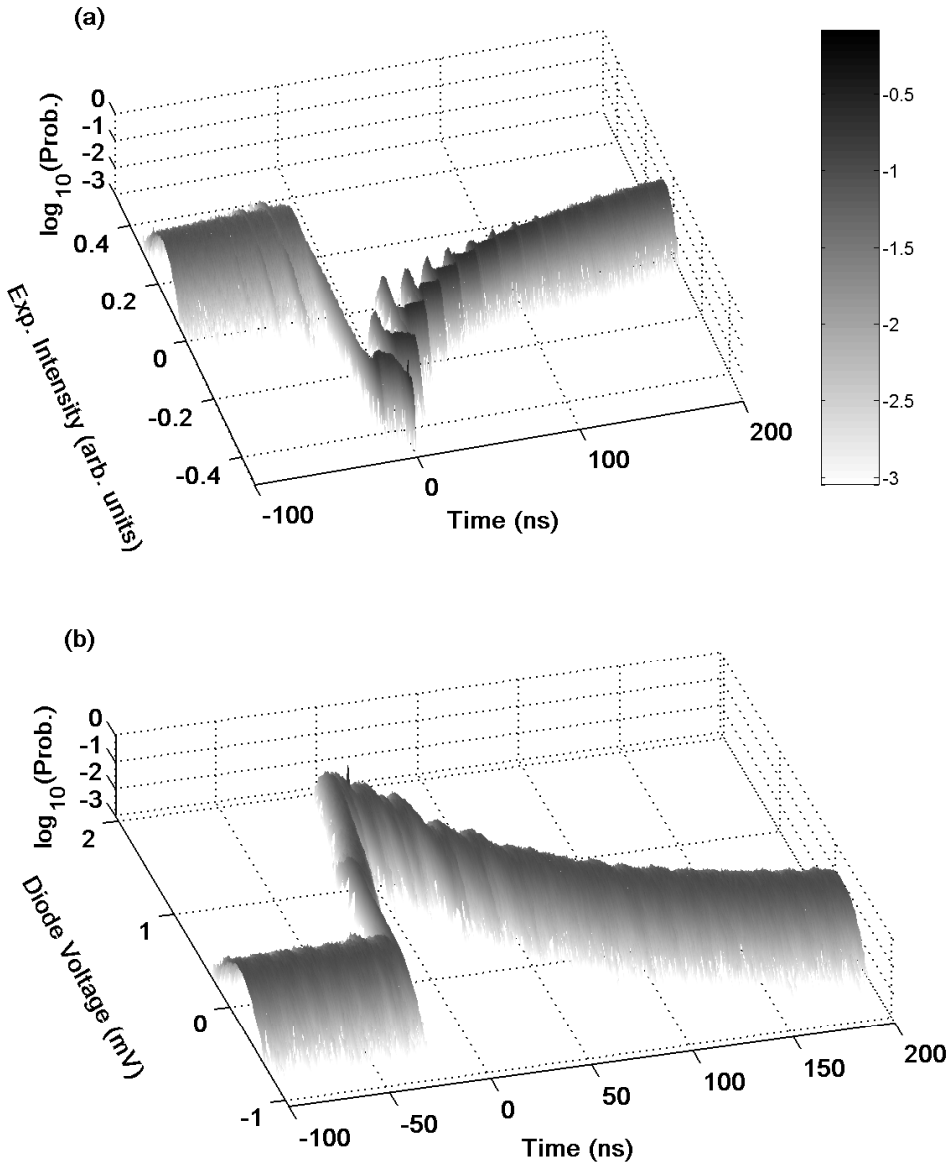

Figure 4.3: (a) The logarithm of the prehistory and posthistory probability distribution function (color coded as shown) of experimental intensity dropouts with $t = 0$ at the bottom of the dropout; (b) the logarithm of the prehistory and posthistory probability distribution of diode voltage pulses corresponding to the intensity dropouts in (a).

connector. In the model RLC circuit C is in parallel to the serial connection of L and R, and the values of L and C are optimally chosen with a resonant frequency of the uncharacteristic 24 ns. A 281 MHz low-pass filter removes high frequencies incurred in the transformation [76].

The prehistory ($t < 0$) and posthistory ($t > 0$) probability distribution functions constructed from 718 intensity dropout events in the experiment are shown in Fig. 4.3(a), where the moment of dropout ($t = 0$) is referenced at the lowest point of a given dropout pulse evolution. The average intensity of the entire time series has been subtracted and the probability of a particular intensity at a given time instant is presented logarithmically to clearly display the variation of trajectories outside the optimal path.

The prehistory distribution reveals the behavior of the system immediately before the dropout. Far from the dropout, there is no structure in the dynamics, and the optimal path lies along the average maximal output. Right before the intensity drops, however, several periodic build-up spikes are visible with a period which is one external cavity round trip time. In the posthistory distribution, a stair structure is clearly visible with a stair width of one round trip time [73]. As the intensity recovers close to the maximal output region, the stairs become indistinguishable.

Fig. 4.3(b) displays the prehistory and posthistory distribution for the pulses of the deconvoluted diode voltage corresponding to the intensity dropouts in Fig. 4.3(a). In the prehistory, no build-up structure may be resolved, and we observe a rise in the pulse to full height. The posthistory distribution shows the gradual decay of the voltage fluctuation, modulated at the round trip time period.

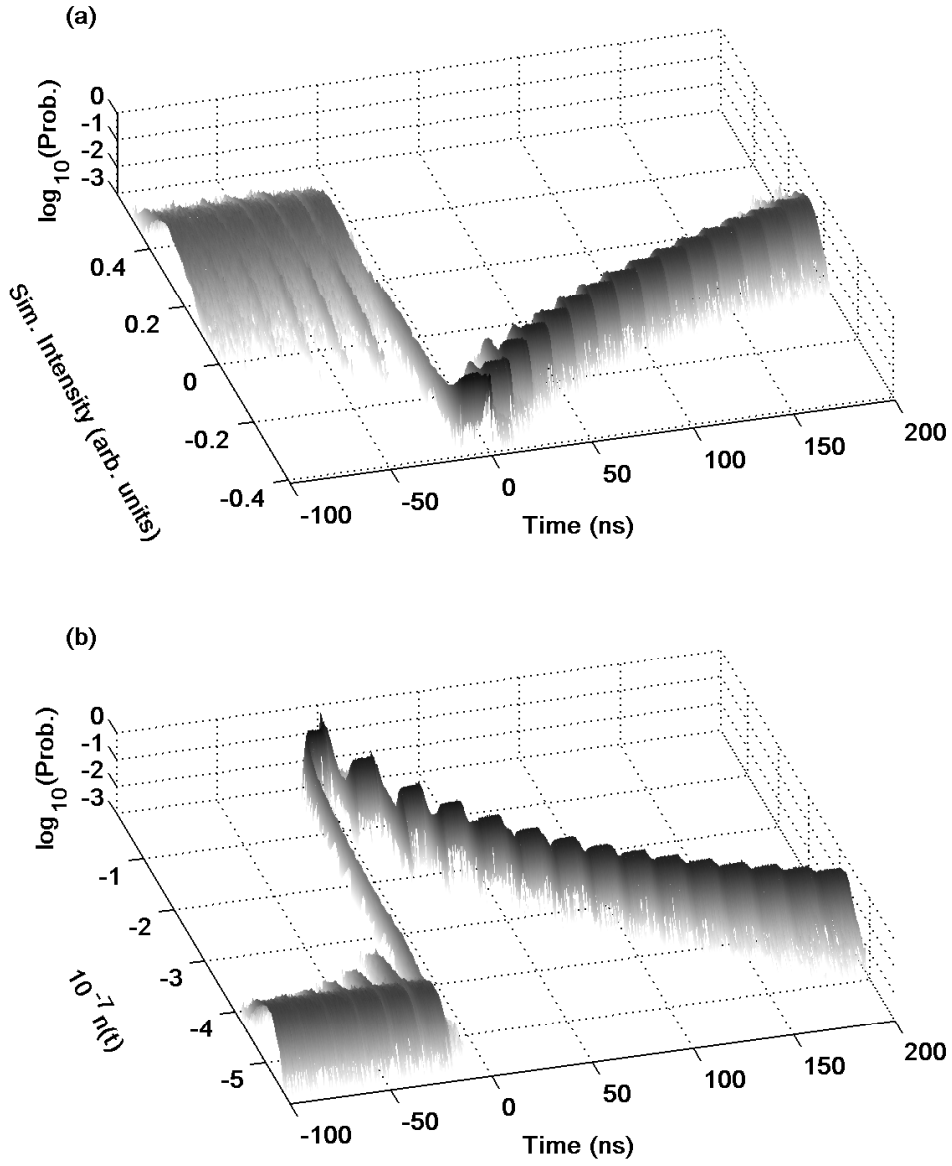

Figure 4.4: (a) The logarithm of the prehistory and posthistory probability distribution of simulated intensity dropouts; (b) the logarithm of the prehistory and posthistory probability distribution of carrier number difference corresponding to the intensity dropouts in (a).

The experiment may be numerically modeled by integrating Eqns. 2.18 with a time step of 0.5 ps for the following parameter values: $N_{th} = 3.3 \times 10^8$, $\beta_c = 5$, $G_N = 7176\ s^{-1}$,$\tau = 14.2\ ns$, $R_{sp} = 5 \times 10^{13}\ s^{-1}$, $\tau_r = 1.1\ ns$, $\Gamma = 1.2\ ps^{-1}$, $\kappa = 2 \times 10^{11}\ s^{-1}$, $P = 1.01$. The calculations are low-pass filtered and smoothed over intervals of 0.2 ns to simulate the digital oscilloscope electronics.

In Fig. 4.4, the prehistory and posthistory distributions for the intensity and the carrier number from the simulation are plotted. In Fig. 4.4(a), all structures shown in the experimental distribution of Fig. 4.3(a) are accurately reproduced. The distribution in Fig. 4.4(b) clearly depicts the characteristic stair structure and periodic build-up spikes. The flat portions of the optimal trajectory for the distributions in Fig. 4.3 and Fig. 4.4 correspond to the residence of the system in an external cavity mode. However, at intervals of the external cavity round trip time, the optimal path demonstrates large swings which indicate the most likely excursion taken by the system variables in transit to the next low-dimensional lasing mode.

4.4 Discussion

In Fig. 4.5(a), we build the phase space dynamics from the experiment using the optimal intensity and deconvoluted diode voltage from the distributions in Fig. 4.3. Similar dynamics are constructed in Fig. 4.5(b) using the optimal intensity and carrier number from Fig. 4.4. The modes (blue triangles) and antimodes (red circles) in this representation lie interlaced along a curve. Before the dropout, the trajectory resides in the high gain modes at the top of the curve. The trajectory

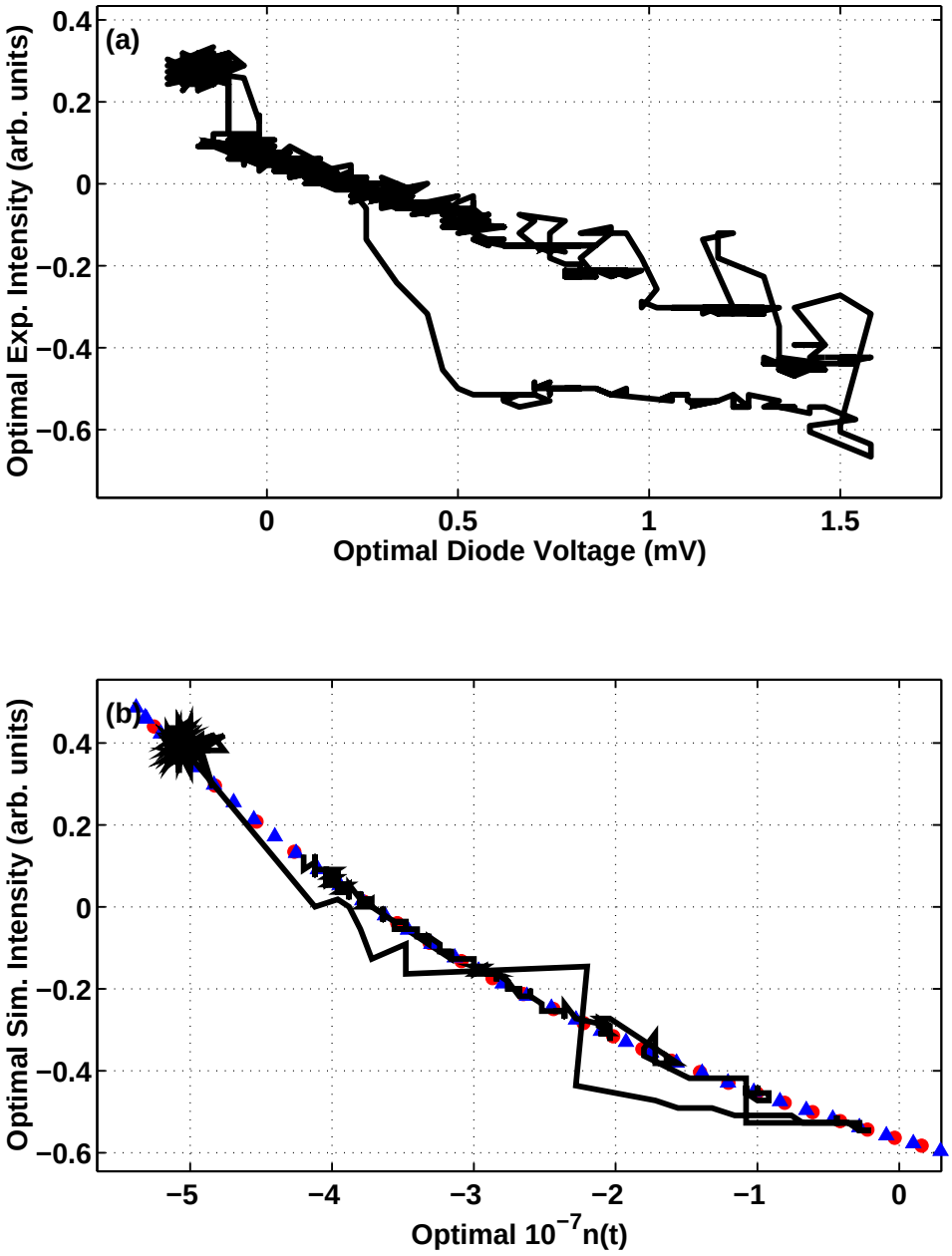

Figure 4.5: (a) Experimental dynamics in the phase space of optimal measured dropout intensity versus diode voltage, (b) computational dynamics in the phase space of optimal simulated dropout intensity versus deconvoluted carrier number difference. The blue triangles represent external cavity modes and the red circles denote antimodes of the Lang-Kobayashi equations.

traverses the phase space during the pulse and iteratively recovers along a series of external cavity modes, clearly depicting in-step itinerant transitions of the intensity and carrier dynamics.

The simultaneous transitions between the system variables may alternatively be visualized in a time-delayed embedding of the optimal intensity path derived from the distributions. In Fig. 4.6 (a) a three-dimensional representation of the recovery process is presented in the phase space of the optimal experimental intensity and two delayed coordinates. A consideration of the first minimum of the mutual information of the optimal path reveals that the least amount of general correlation is found for $\tau_{DLY} = 0.5\ ns$. The reconstructed attractor demonstrates a strong localization of the delayed coordinates when the laser is locked to a step. At intervals of the external cavity round-trip time, however, the light dynamics perform a large oscillation in transit to the next recovery step. Similar features may be deduced from the time-delayed embedding of the simulated optimal intensity depicted in Fig. 4.6 (b).

During an itinerant epoch, the system variables released from a local attractor are temporarily free to occupy a larger volume of phase space until the system locks onto another low-dimensional external cavity mode. The increase in available system phase space results in a significant broadening of the probability distributions computed for measurements of the light intensity and carrier number. This variation is illustrated concretely in Fig. 4.7, where we plot the time dependence of the standard deviation of the measured and calculated distributions in Fig. 4.3 and Fig. 4.4. Sharp rises in the standard deviation of the distributions occur at intervals of the external cavity round trip time, where high-dimensional dynamics dominate

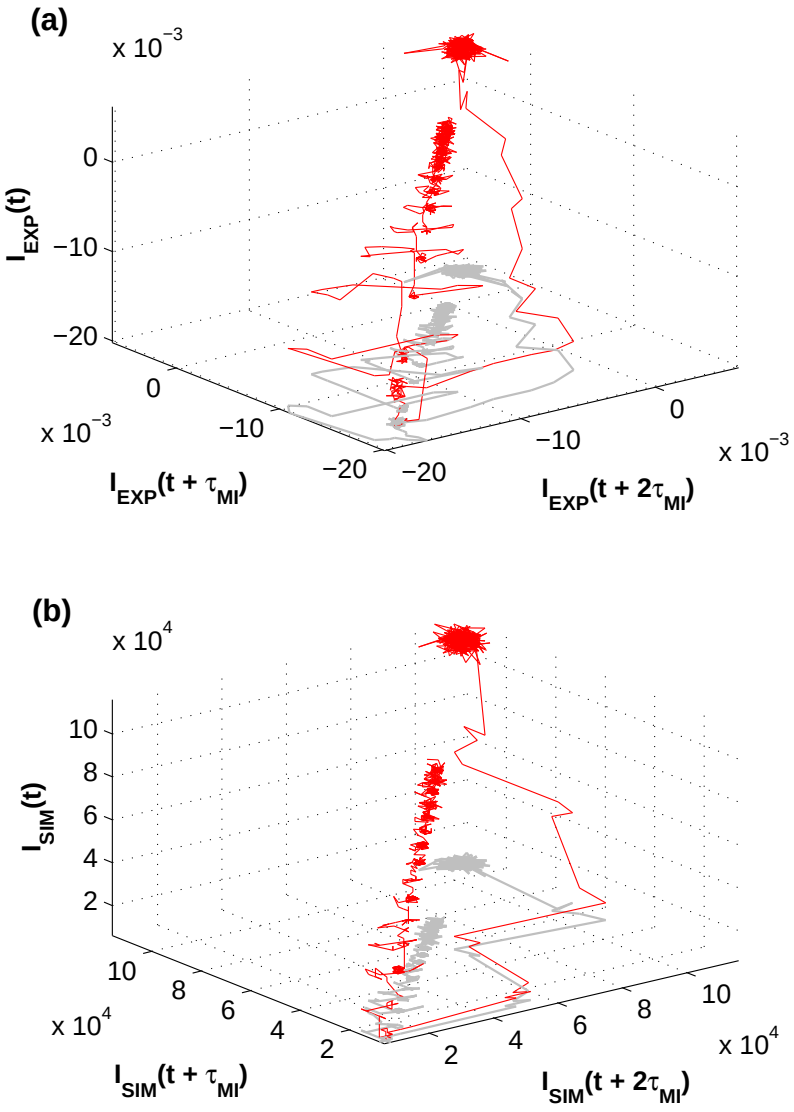

Figure 4.6: The attractor reconstructed from a time-delayed embedding of the (a) experimental and (b) simulated optimal path. In each case the mutual information provides an ideal delay time of $\tau_{DLY} = 0.5\ ns$

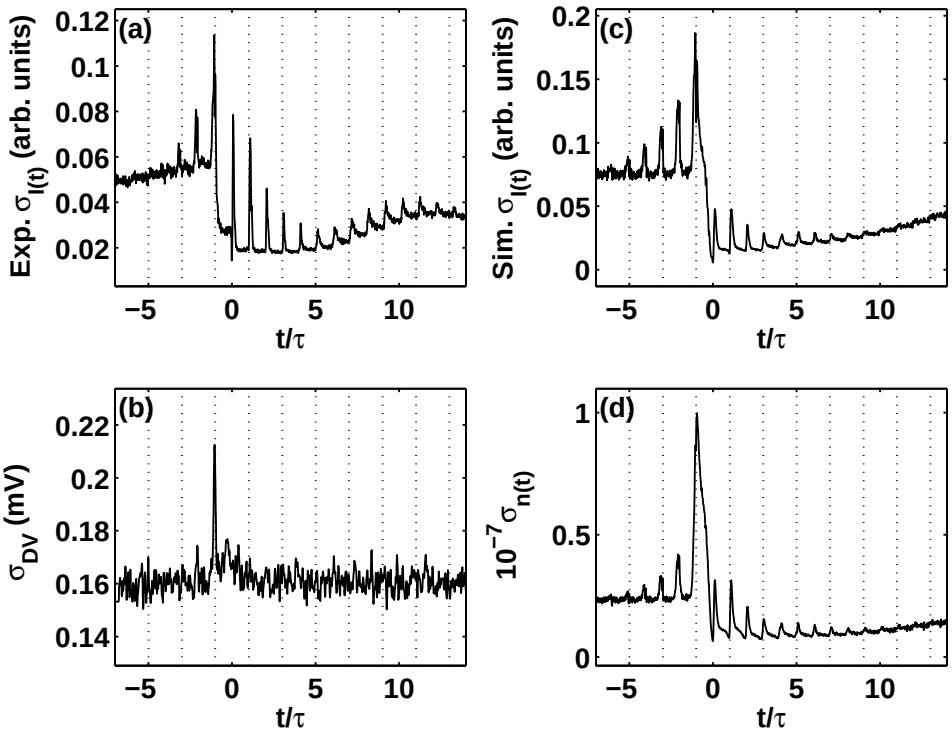

Figure 4.7: The standard deviation σ of the probability distributions of (a) experimental intensity dropouts, (b) diode voltage pulses, (c) computational intensity dropouts, and (d) carrier number difference. Time is displayed in units of the external cavity delay time τ.

the motion of the feedback system. These distributions show that itinerant motions are present both before and after the dropout events. This observation cannot be explained by a simplified one dimensional stochastic model [48, 35] of fluctuation-induced escape. The deterministic structure observed before the dropout implies that the itinerant deviations are reinforced over many round trip times until the dropout finally occurs.

4.5 Conclusions

We have reported experimental observations of concurrent itinerant motions in the light and carrier dynamics of a semiconductor laser under the influence of reflective feedback. These measurements are consistent with the predictions of the Lang-Kobayashi equations. The role of chaotic itinerancy in the time evolution surrounding an intensity dropout is evaluated in detail using prehistory and posthistory probability distributions calculated from experimental measurements of the intensity and voltage fluctuations across the diode. At intervals of the external cavity round trip time, the system variables are no longer locally constrained to a low-dimensional external cavity mode. Despite this loss of coherence in the light and carrier dynamics, a continuous optimal path of escape to another attractor ruin is evidenced in the reconstructed phase portrait of the dropout process. This path demonstrates a certain determinism of motion through high-dimensional phase space in the dynamics of a time-delayed experimental system that is additionally influenced by noise.

Chapter 5

Noise-Induced Selection of the Light Dynamics

Near lasing threshold, a semiconductor laser displays irregular dropouts of the intensity over a wide range of feedback strengths. As we saw in the previous chapter, the optical intensity recovers from these dropouts (LFFs) in a stepwise manner over a time scale which is much longer than the laser system dynamics. When the injection current is raised well above threshold, however, the intensity dropouts are no longer present and the light dynamics show pronounced large amplitude chaotic fluctuations characteristic of the coherence collapse (CC) regime [50].

Generally, these two instabilities are studied individually at injection currents and feedback strengths well within either the LFF or CC regime. Only a few investigations have examined this system at intermediate parameter values near the boundary between these chaotic states. Previous studies have mapped out the parameter space where each dynamical state is stable [77] and have characterized changes in the interval between dropouts for variations of the injection current [78, 79]. It is well-documented that spontaneous emission plays a non-trivial role in shaping the dynamics of the laser system, particularly at injection current strengths near the solitary lasing threshold where the LFF attractor is dominant. The inclusion of stochastic terms in simulations has been shown to be instrumental in order to match the duration between dropout events and power spectrum fluctuations which

appear in experimental observations [**?**].

In this chapter we quantitatively examine, for a fixed level of reflective feedback, the stability of the LFF and CC state over a large range of injection currents for different amplitudes of noise. A consideration of the Lang-Kobayashi model without Langevin noise shows that an intermittency exists between LFF and CC over a wide span of injection currents, including pump strengths below the solitary lasing threshold. The addition of noise resticts the itinerant pathways leading to CC dynamics at low injection currents, creating regions where the LFF state dominates the system dynamics. As noise is further increased in the model, the LFF is preferentially selected over the CC state for larger spans of the injection current. The constructive role of this stochastic influence complements other studies of high-dimensional nonlinear dynamical systems which have observed a noise-induced selection of otherwise weak attracting states [39, 40].

Even though noise stabilizes the LFF state at low pump currents, we experimentally and numerically witness a similar intermittent transition to CC as the injection current is incremented beyond a critical threshold. This threshold is shown to follow a power law scaling in the simulations with respect to the noise level over many orders of magnitude. Noise effectively translates the region over which this intermittency occurs to higher levels of the injection current. An experimental characterization of the intermittency then offers a meaningful estimation of the noise level which effectively influences the deterministic dynamics in this system.

5.1 Noise-Induced Suppression of the Coherence Collapse Regime: Numerical Simulations

We first consider the dynamical states predicted by the Lang-Kobayashi model without the influence of a stochastic term ($R_{sp} = 0$) at a fixed level of moderate feedback which reduces the threshold current of the laser 7%. Eqns. 2.19 and 2.20 are integrated with a time step of 1 ps (photon decay rate) for the following parameter values: $\alpha = 4.6$, $\theta = 14.2\ ns$, $\kappa = 0.073$, $T = 1500$. Over a wide range of injection currents the LFF state is observed to coexist with another dynamical state. For injection current levels lower than $p = -0.025$ the LFF state only exists as a transient and the system trajectory will eventually be captured by the stable maximum gain mode at the tip of the ellipse [80] formed by the modes and anti-modes in the phase space of the carrier number and the external cavity phase shift. Even at these low pump values the LFF state is occasionally interrupted by bursts from another dynamical state resembling CC dynamics. Above $p = -0.025$ the intermittency between the two dynamical states is observed to persist with more frequent departures to the CC regime.

In Fig. 5.1 the light dynamics are seen to alternate between LFF and CC dynamics at an injection current of $p = 0$ (solitary lasing threshold). The intensity time trace in Fig. 5.1 (a) has been low-pass filtered at 50 MHz to remove resonances associated with the external cavity round trip time (70 MHz) and more easily discriminate between the two dynamical states. Large dropout pulses of the LFF state are sporadically punctured by rapid oscillations of the CC regime. As discussed

in Chapter 2 these globally attracting states are formed from characteristic interactions between the external cavity modes and antimodes. The time trace of the external cavity phase shift $\eta(t)$ in Fig. 5.1 (b) highlights the signature transitions between the external cavity modes (separated by 2π) for each dynamical state. The dropouts of the LFF state only occur at external cavity modes near the maximum gain mode and are followed by a slow monotonic recovery. In the CC state, the orbit of $\eta(t)$ is instead restricted to a subset of the external cavity modes. Here the push towards the maximum gain mode is frustrated by frequent slips of $\eta(t)$ to lower mode numbers. More pathways to lower mode numbers are available at larger injection currents and LFF phenomenon is no longer present for $p > 0.06$.

Without a stochastic term in the model equations, both the LFF and CC states are available to the system over a wide range of injection currents. We now consider how the dynamics of the laser system are affected by the addition of Langevin noise. As the amplitude of the noise is incremented for a fixed level of feedback and injection current, we evaluate how noise shapes the preference of external cavity modes by the system as well as the transitions observed to occur between them. Ultimately, these features determine the dynamical states accessible to the system over variations of a system parameter.

In Fig. 5.2 we plot the distribution of external cavity mode residence times for increasing levels of the noise amplitude at an injection current level of $p = 0.05$. All other system parameters are the same as those considered for the noiseless case. Without noise, the light dynamics overwhelmingly exist in the CC state, and the distribution of the external cavity modes (blue line) demonstrates a broad Gaussian

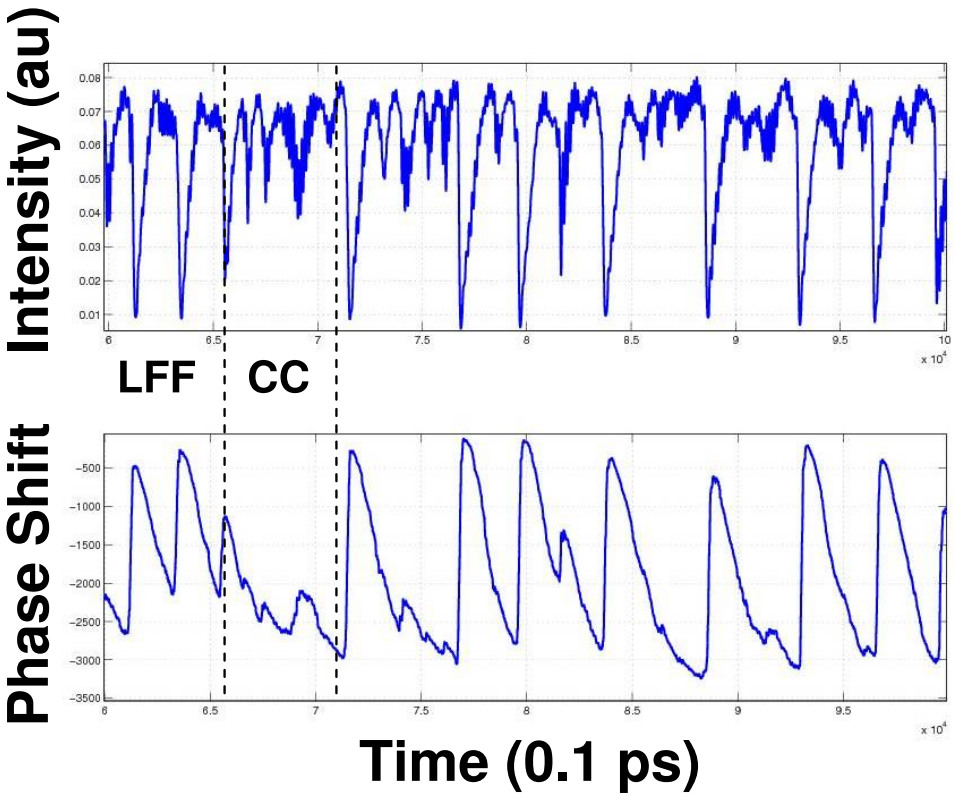

Figure 5.1: The top panel features a severely filtered (50 MHz) intensity time trace in order to smooth the dynamics sufficiently so that full dropouts may be resolved from the incomplete bursts to the CC state. The lower panel shows the time trace of the external cavity phase shift $\eta(t) = \phi(t) - \phi(t-\tau)$. Note that jagged motions in $\eta(t)$ reflect the CC dynamics and occur in intervals where the incomplete dropouts are prevalent.

peak centered halfway between the solitary lasing frequency and the maximum gain mode. At a noise level of $R_{sp} = 1 \times 10^{-6}$, an asymmetry develops in the distribution (green line) towards the maximum gain mode, although a wide peak remains. When the noise amplitude is increased to $R_{sp} = 1 \times 10^{-4}$, two narrow peaks are evident in the distribution (red line), each centered at external cavity modes which are unavailable to the system without the inclusion of noise.

The distributions in Fig. 5.2 clearly indicate that the noise amplitude dictates which external cavity modes are visited by the system. They do not provide any information, however, on the transitions which occur between individual external cavity modes. In Fig. 5.3 the evolution of the system in the phase space of the carrier number and external cavity phase shift is plotted for respresentative trajectories of the three noise levels considered in Fig. 5.2. The red crosses denote the external cavity modes and the blue circles designate the antimodes. When there is no stochastic term present in the model equations, the orbit in Fig. 5.3 (a) exhibits back-and-forth transitions between widely separated external cavity modes. The external cavity phase shift does not stray towards either the maximum gain mode or solitary lasing conditions, a signature of CC dynamics observed in Fig. 5.1 (b). In Fig. 5.3 (b), the system similarly exhibits itinerant motions among a subset of external cavity modes for a noise amplitude of $R_{sp} = 1 \times 10^{-6}$, although now the LFF trajectory emerges along with a damping of the carrier number fluctuations. The damping of the carrier fluctuations is even more extreme in Fig. 5.3 (c) for a noise level of $R_{sp} = 1 \times 10^{-4}$. In the full LFF phenomenon massive shifts in $\eta(t)$ all redeposit the system near solitary lasing conditions. The nadir of the dropout

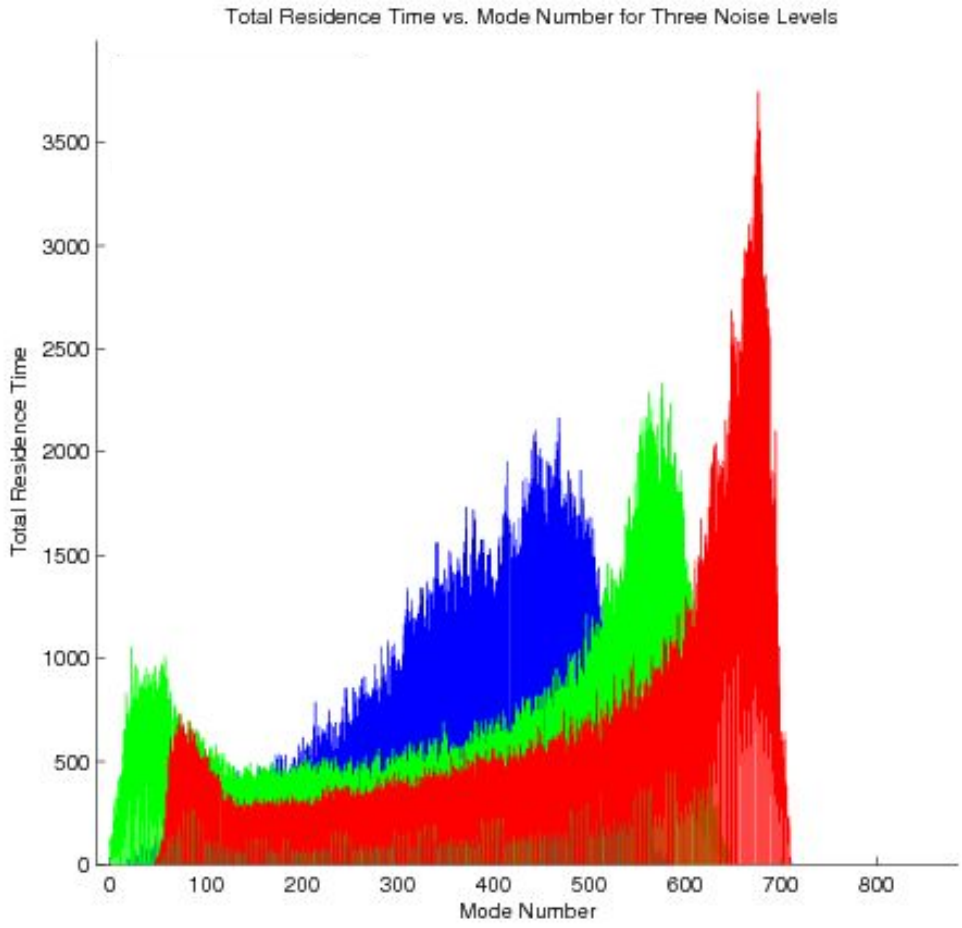

Figure 5.2: The three distributions of external cavity mode times represent the noise amplitudes discussed in the text: (1) $Rsp = 0$ (blue distribution), (2)$Rsp = 1 \times 10^{-6}$ (green distribution), and (3)$Rsp = 1 \times 10^{-4}$ (red distribution). Here the mode number is defined as the division of the external cavity phase shift by 2π (the inherent spacing between pairs of modes).

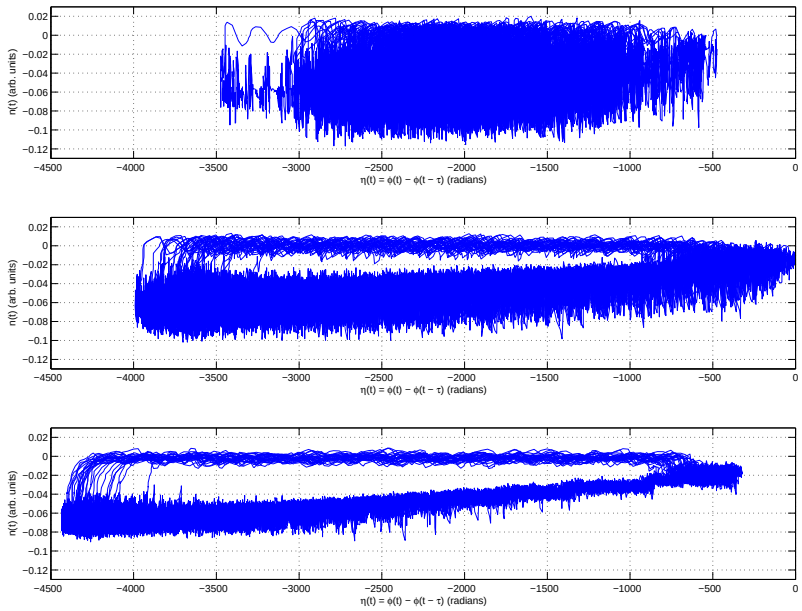

Figure 5.3: For the three manifestations of noise in Fig. 5.2, the trajectory in the phase space of the external cavity phase shift and the carrier number more closely resemble the LFF dyamics as noise is incremented for (from top to bottom) $R_{sp} = 0$, $R_{sp} = 1 \times 10^{-6}$, $R_{sp} = 1 \times 10^{-4}$.

comprises the secondary peak near solitary emission observed in the distribution (dotted lines) of Fig. 5.2 (b),(c).

As the noise amplitude is increased in the model, itinerant pathways characteristic of CC emission are suppressed in the system. Even for small levels of noise, there exists a range of injection currents where no intermittency persists in the dynamics and LFF is the only dynamical state observed in the system.

In Fig. 5.4 we plot the logarithm of the highest level of injection current where the LFF state is uniquely observed in the system, denoted by p_c, against the

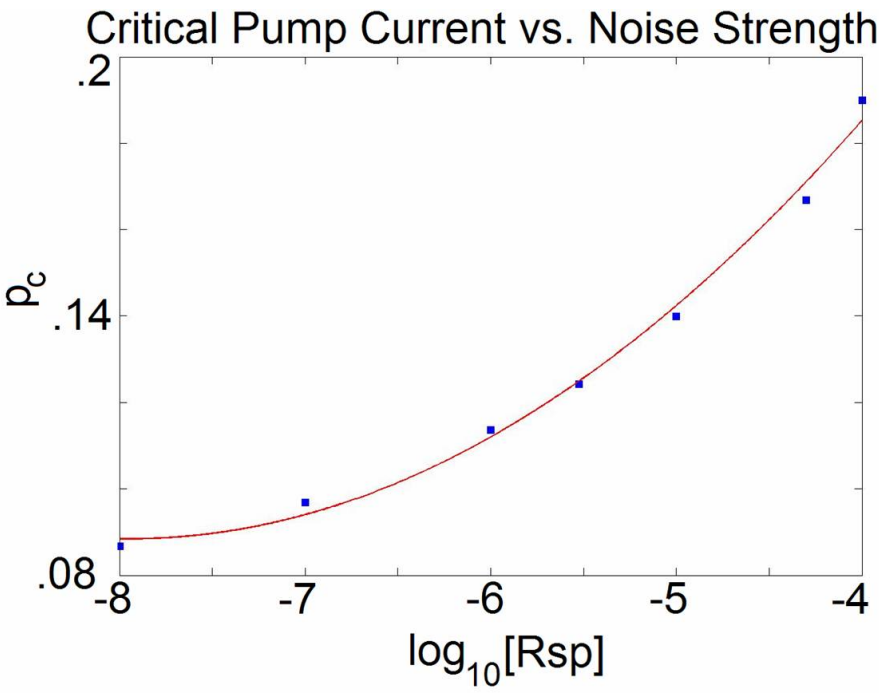

Figure 5.4: The highest injection current where the LFF region is stable p_c increases monotonically when plotted against the logarithm of the noise amplitude. Here the onset is measured with respect to the lasing threshold in the presence of feedback.

logarithm of the underlying noise level. The injection current is evaluated relative to the threshold level for lasing emission in the presence of feedback at $p = -0.07$. Beginning with its emergence around $p = -0.03$, the LFF state is found to be the only attracting state for larger values of the injection current as the noise amplitude is incremented.

5.2 Intermittency Characteristics

The previous section explored the role that additive noise plays in selecting the dynamical states observed in a semiconductor laser with coherent optical feedback.

The LFF state is rendered stable over a finite span of the injection current due to the suppression of CC itinerant pathways. This span grows to higher levels of the injection current as the noise amplitude is increased. We now address the inevitable breakdown of the LFF state as the injection current is increased beyond the region of noise-induced stability. When the injection current is tuned past a critical value, the LFF dynamics are punctured by intermittent episodes of CC dynamics similar to computations of the model equations without a stochastic term. This phenomenon is explored experimentally and in simulations of the Lang-Kobayashi model with Langevin noise. Even in the presence of spontaneous emission noise in the laser cavity, the average time between CC bursts demonstrates a clear algebraic scaling as the injection current is increased beyond the level where intermittency is observed. We will show in the simulations that over many orders of magnitude of the noise, the characteristic scaling law associated with each noise amplitude collapses onto a single curve when the injection current is taken relative to the onset threshold of the intermittency.

The experiment is conducted using a Fabry-Perot semiconductor laser (RLT8438) with a threshold current of $I_{th} = 48.2\ mA$. The setup is the same as in Fig. 2.6 except here an etalon was positioned in the delay loop to restrict the laser oscillations to a single longitudinal mode at $\lambda = 830.5\ nm$.

In Fig. 5.5 we show the evolution of the intensity for increasing levels of injection current I at a feedback strength which reduces the lasing threshold by 8%. As depicted in Fig. 5.5 (a), the intensity exhibits power dropouts at a driving current of $I = 52.0\ mA$. LFF dominate the light dynamics until I is increased past a

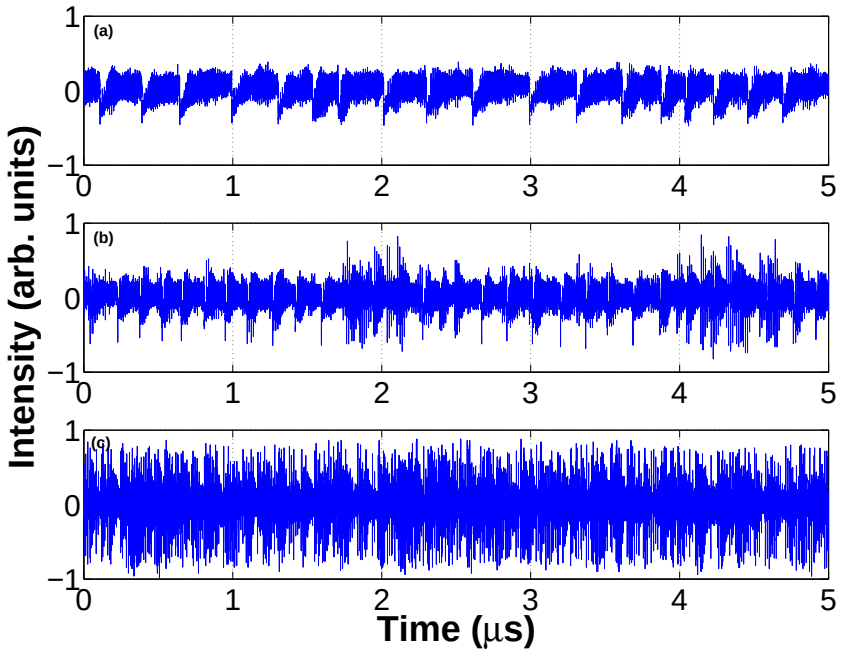

Figure 5.5: The light dynamics measured in the experiment display intermittency between the LFF attractor and more complicated fluctuations resembling CC dynamics at (a)$I = 52.0\ mA$, (b)$I = 56.0\ mA$, and (c)$I = 65.0\ mA$.

threshold level $I^* \approx 53.0\ mA$. For injection current levels larger than I^*, the power dropouts demonstrate an intermittency with a new attracting state. In Fig. 5.5 (b) this bursting behavior is demonstrated for $I = 56.0\ mA$. For further increments of I, the system resides entirely in the bursting state with even larger oscillations in the light dynamics, shown in Fig. 5.5 (c) for $I = 65.0\ mA$. We note that the I^* is strongly dependent on the feedback strength, and the LFF regime remains stable for higher levels of I as the feedback is augmented [77].

The power spectra measured from the intensity time traces of Fig. 5.5 are displayed in Fig. 5.6. In Fig. 5.6 (a) a majority of the power is found in the low-

frequency component of the dropout pulses. The smaller peaks at higher frequencies are associated with the external cavity round-trip time and its harmonics. When intermittency appears in the intensity time traces and fast, large-amplitude swings of the intensity are present, as in Fig. 5.5 (b), the bursts contribute energy to the power spectrum in Fig. 5.6 (b) at the peaks associated with the delay cavity. The low-frequency component is not as dominant in the spectrum as it is in Fig. 5.6 (a). Finally, when the system resides entirely in the CC state, the power spectrum in Fig. 5.6 (c) shows a concentration of energy at the peaks of the delay cavity with no trace of the low-frequency component of the LFF attractor. For an intermittency found in a periodically driven CO2 gas laser [81], the original attractor and the bursting state similarly produced unique frequency signatures in their respective power spectrum. Arecchi and co-workers have demonstrated that the bursts are preventable in their system by selectively filtering out the frequency content of the bursting attractor [81].

To characterize the intermittency in the light dynamics, we examine the residence times of the system on the original LFF state for injection currents near the onset of intermittency. In Fig. 5.7 we plot the average interburst times as a function of the injection current for the experimental data (red circles). These times are seen to rapidly decrease as the injection current is incremented. The vertical asymptote I_c represents the onset of intermittency and its choice will become more clear when we examine the scaling associated with the introduction of the bursts.

For each deviation of the injection current past I_c, denoted $\Delta I = (I - I_c)/I_c$, the probability distribution of the interburst times τ is seen to follow an exponential

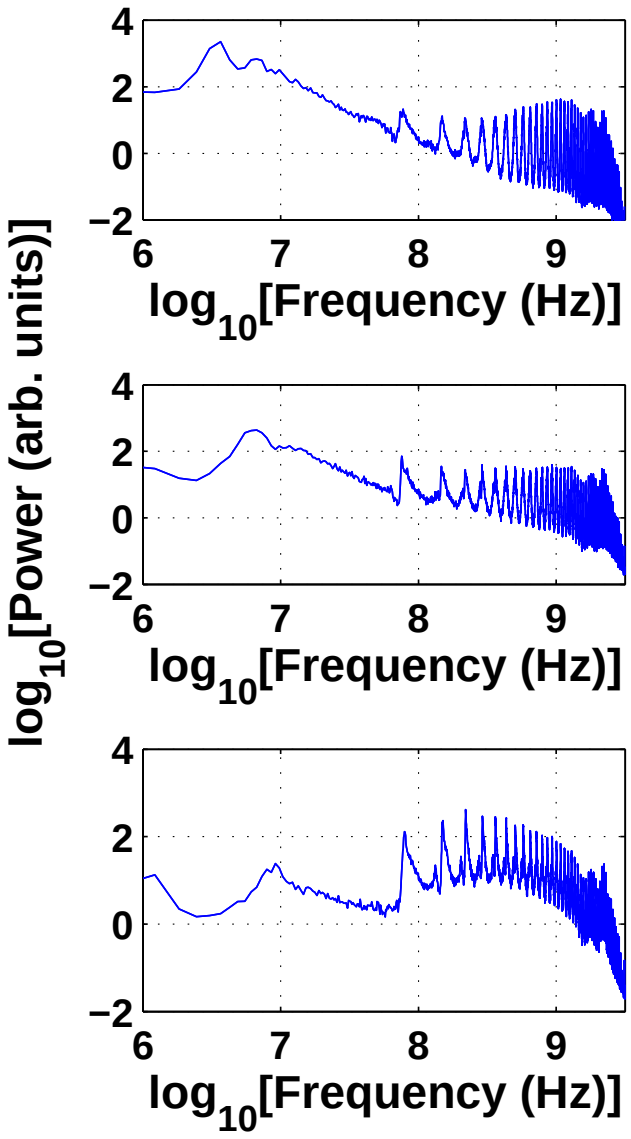

Figure 5.6: The experimental spectra corresponding to the three intensity time series shown in Fig. 5.4. Note that before the bursts (top panel) a large low-frequency component is visible in the spectrum in the low MHz range. The magnitude of this peak decreases (along with an increase in the external cavity resonances) for increasing pump strength which intermittently introduces the CC regime.

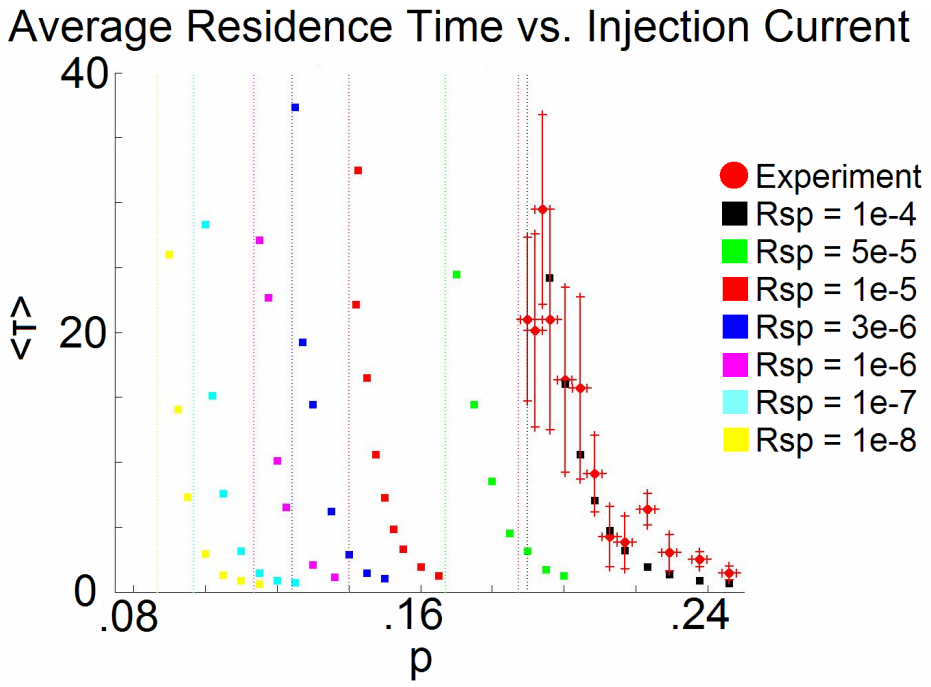

Figure 5.7: The average interburst time $< \tau >$ is plotted against the raw injection current for experiment (red circles) and many noise amplitudes in the simulation (squares). The simulation points clearly show the increase of the range of injection current where the LFF region is stable as the noise amplitude is incremented.

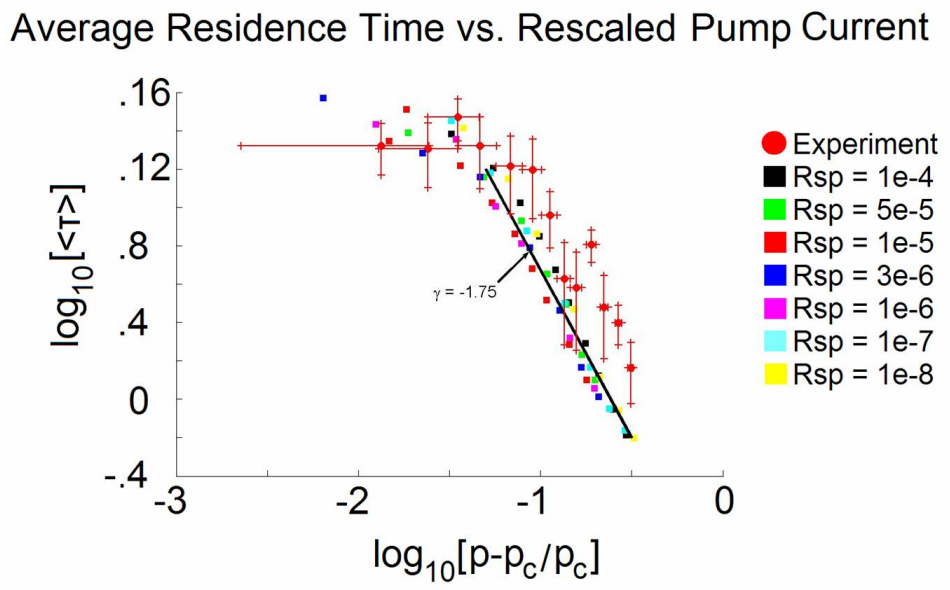

Figure 5.8: The logarithm of the average interburst time $< \tau >$ is plotted against the logarithm of deviations of the injection current from the onset of intermittency ΔI for experiment (red circles) and many noise amplitudes in the simulation Δp (squares). The simulation points clearly collapse onto a single curve with a scaling exponent of $\gamma_{SIM} = 1.75$ while the scaling exponent of the experiment is $\gamma_{EXP} = 1.64$.

decay. The LFF dynamics are interrupted more frequently for larger ΔI. The experimental points (red circles) in Fig. 5.8 show that the average interburst time $< \tau >$ decreases with ΔI according to a power law decay. Eight 1.6 ms samples are recorded for each ΔI to estimate $< \tau >$. The value of $I^* = 53.1$ mA was chosen as the injection current value where an extrapolation of the points on the graph of $\log(< \tau >)$ vs. $\log(\Delta I)$ predicts that one event will occur in a 1.6 ms sample and results in a scaling exponent of $\gamma_{EXP} = 1.64$.

With the inclusion of the Langevin noise term, at several fixed levels of feedback the Lang-Kobayashi equations robustly reproduce the intermittent transition observed in the experiment. In Fig. 5.9 the light dynamics generated from the model are displayed at a noise strength of $R_{sp} = 1 \times 10^{-4}$. The calculations are low-pass filtered at 750 Mhz and smoothed over intervals of 0.1 ns to simulate the digital oscilloscope electronics. The pump strengths represented in Fig. 5.9 (a)-(c) are matched to the experimental measurements of Fig. 5.5 (a)-(c) and show similar trajectories of the system at each level of injection current. The intensity at $p = 0.120$ in Fig. 5.9 (b) portrays clear escapes to a bursting state, and at a larger pump value of $p = 0.349$ the system dynamics are dominated by the high-frequency large amplitude oscillations depicted in Fig. 5.9 (c). Similarly, the power spectra for the intensity time traces show a clear progression from the low frequencies of the dropouts to a sole distribution of the energies along the frequencies associated with the resonances of the external cavity delay time.

We now evaluate the effect of the stochastic driving term on the scaling of the intermittent transition for various manifestations of noise. For this analysis we computed 1.6 ms samples at several levels of injection current near the onset of this phenomenon for the noise levels considered in Fig. 5.4. In Fig. 5.7 the boundary of the injection current range where the LFF region is stable is observed to increase (squares) as in Fig. 5.4. Once the CC regime is introduced, a similar progression to shorter interburst times of the LFF state is seen in all instances of noise as the injection current is further increased. To evaluate the scaling associated with each noise amplitude, in Fig. 5.8 we plot the logarithm of the average interburst

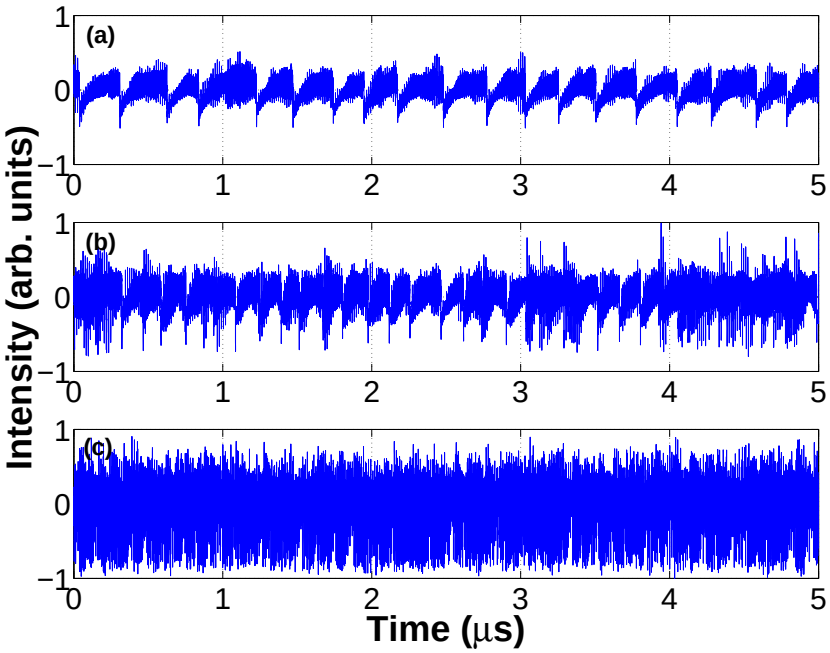

Figure 5.9: The transition to CC dynamics in the simulation for parameters comparable to experimental data shown in Fig. 1 at pump levels of (a)$p = 0.078$, (b)$p = 0.120$, and (c)$p = 0.349$.

times against the respective deviation of the injection current past the onset of intermittency p_c, denoted $\Delta p = (p - p_c)/p_c$. It is clear from this plot that the scaling for each instance of noise (squares) collapses onto a single curve. This gives a strong indication that the noise effectively translates the region of intermittency and expands this region proportionally with the increase of the onset of intermittency and results in a universal scaling exponent of $\gamma_{SIM} = 1.75$. For noise amplitudes less than $R_{sp} = 10^{-8}$ it is too difficult to discern between the LFF and CC dynamics to capture an accurate measure of the interburst times.

5.3 Discussion

Noise has been shown to act as a stabilizing force for the LFF state. In general, the LFF state persists over a larger span of the injection current as higher amplitudes of noise are introduced into the system. The noise effectively translates the region of coexistance between the LFF and CC states to higher values of the injection current. The influence of noise in the system is diminished as the injection current is tuned further from threshold and the CC dynamics eventually dominate the output of the system.

We now consider how the CC state originates in the context of the experimental data and simulations of the model equations with noise. In Fig. 5.10 we show detailed intensity time traces from the experiment and the simulation with a noise level of $R_{sp} = 1 \times 10^{-4}$ for (a) LFF at $p = 0.078$ in the experiment and in the simulation, (b) the bursting dynamical state which inturrupts the LFF dynamics just past the

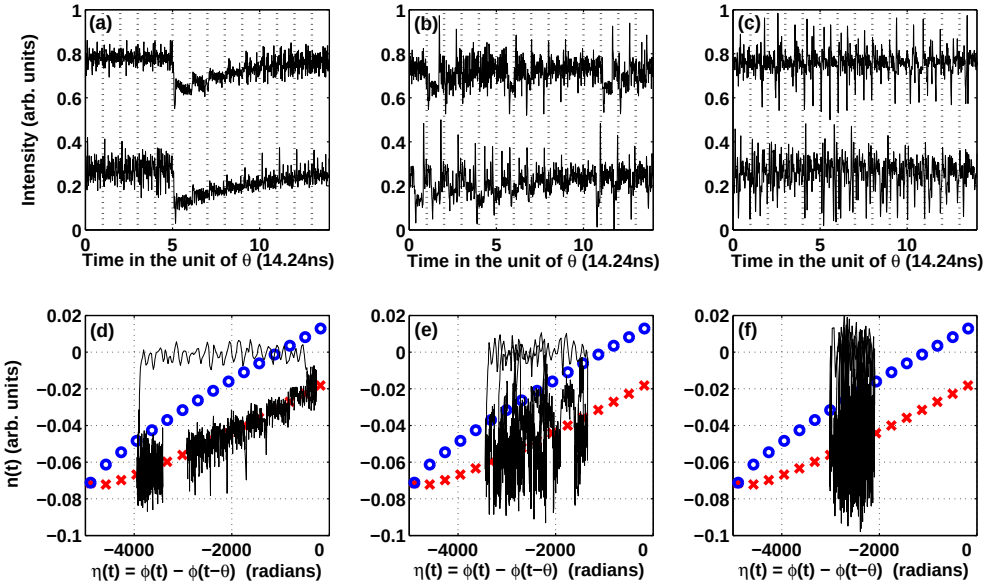

Figure 5.10: Detailed intensity time traces from experiment and simulation at respective pump currents (a) $I = 52.0\ mA$ and $p = 0.078$, (b) $I = 54.0\ mA$ and $p = 0.120$, (c) $I = 60.0\ mA$ and $p = 0.2450$. Experimental traces are offset above the numerically computed time series and the normalization in (a)-(c) is applied to each plot individually to maintain clarity in the intensity dynamics. In (d)-(f) the $(\eta(t), n(t))$ phase space is shown for corresponding simulated intensity dynamics of (a)-(c). The red crosses represent external cavity modes and the blue circles denote the unstable antimodes.

onset of intermittency at $p = 0.120$, and (c) the fully developed CC state for a large pump strength of $p = 0.245$. In each plot the light dynamics recorded from the experiment are offset above the numerically determined time series. The phase space of the carrier number and external cavity phase shift for the simulated trajectories in Fig. 5.10 (a)-(c) are shown in (d)-(f). The red crosses represent the external cavity modes and the blue circles denote the antimodes.

For the experimental and simulated LFF state shown in Fig. 5.10 (a), the intensity time series is seen to suffer a dropout and subsequently recover to maximum gain in a series of steps. The width of each step coincides with the duration of ejected light in the external cavity formed by the reflective mirror. In Fig. 5.10 (d) the moment of dropout results in an immediate rise of the carrier number to threshold level and, over an interval of the delay time, a relaxation of the external cavity phase shift above the antimodes towards solitary lasing conditions ($\eta = 0$). The recovery towards maximum gain then takes place along the external cavity modes on the lower branch of the ellipse.

On the other hand, the light dynamics of the time series in Fig. 5.10 (b) demonstrate rapid changes in the intensity output. Although there are clear similarities to the dynamics of the LFF attractor, this dynamical state alternates between high and low levels of emission *within* an interval of the external cavity delay time. To understand this novel switching behavior, we turn to the phase portrait in Fig. 5.10 (e). In a manner similar with the dropout dynamics, the sharp reduction in output power arises when the system is kicked above the antimodes with a large increase in the carrier number. During the locomotion of the system towards solitary lasing

conditions, however, the trajectory is 'captured' by an external cavity mode with high gain in the middle of the ellipse, coincident with the sudden shift in Fig. 5.10 (b) to a larger intensity. The dramatic changes in the system variables at the moments of dropout and mode-capture are manifested at later intervals of the external cavity round-trip time throughout the remainder of the recovery. The CC behavior is typically sustained for the duration of a few dropout events before the system returns to the original LFF attractor.

It is clear that the injection current plays a crucial role in determining the interaction between the external cavity modes and antimodes. As the laser diode is pumped further from the onset of intermittency, the system trajectory is dominated by these interactions, and regular motions associated with the LFF attractor are replaced by large amplitude swings of the intensity, depicted in Fig. 5.10 (c). The increased interactions among the modes and antimodes in Fig. 5.10 (f) restrict the motions of the system to a narrower range of external cavity modes in the middle of the ellipse and do not allow the full climb down to the maximum gain modes at the tip of the ellipse.

In this particular system noise has the curious effect of stabilizing an attracting state in the system over larger spans of the injection current, preventing the onset of bursts from the CC regime. This is an atypical consequence of stochastic terms in a system exhibiting an intermittency in the dynamics. In crisis-induced intermittency, additive noise has been shown to restrict the range of a parameter where a unique attractor is visited by the system. Stochastic influences additionally affect the characteristic scaling law for the average duration between intermittent episodes

at parameter values in the bursting regime. Theoretical and experimental studies of on-off intermittency have likewise demonstrated that additive noise promotes more frequent departures of a system trajectory to a bursting state.

5.4 Conclusions

We have examined the role of additive noise in selecting the dynamical states observed in a semiconductor laser with time-delayed optical feedback. Analysis of the delay-differential equations governing this system predict a chaotic itinerancy among external cavity modes and unstable saddles, and the overall motions between the attractor ruins generally fall into one of two distinct regimes of chaotic output. We quantitatively characterized an intermittency between these dynamical states over a wide range of a system parameter for different levels of Langevin noise. As higher levels of noise are introduced into the system, the system preferentially selects one of the dynamical states for a larger span of the parameter, preventing the onset of intermittency. Stochastic terms do not have nearly the same impact on the system dynamics at higher pump levels, where the constant current supplied to the laser diode strongly overwhelms the spontaneous emission noise (capped once the laser is tuned past threshold). Hence, the influence of the stochastic driving on the laser decreases as the injection current is raised from threshold.

The characteristic scaling associated with the intermittent transition has been studied experimentally and compared with simulations of the Lang-Kobayashi equations for different manifestations of Langevin noise. The translation of the inter-

mittency region is shown to monotonically increase as a function of the input noise. The experimental characterization of the location and scaling of the intermittency provide a sensitive method for estimating the influence of noise when the dynamics of the system display a chaotic itinerancy.

Chapter 6

Conclusions

In conclusion, we have performed three experiments that measure the influence of noise in a semiconductor laser subject to time-delyed optical feedback from a distant reflector. Once a semiconductor laser is pumped at a high enough injection current to emit stimulated emission, the level of noise in the system is fixed regardless of how much higher the injection current is tuned. As such, the influence of noise is interpreted to be very influential near lasing threshold but is highly diminished as the pump current is incremented.

In the first two experiments, we separately investigated the two dominant regimes of chaotic behavior with a different motivation in measuring the influence of noise. Specifically, at the high injection currents which produce the coherence collapse (CC) regime of chaotic behavior, we addressed the question of whether spontaneous emission contributes at all to the dynamical evolution of the system over a range of feedback strengths. As an estimator of the influence of noise, we calculated the Hurst exponent from associated phase fluctuations of the experimental and simulated intensity time series. To access physically meaningful phase fluctuations we utilized an empirical mode decomposition along with the Hilbert transform. We found that a scaling exists for time scales slower than the external cavity round trip time of the light and it demonstrates a transition to fractional Brownian motion in

the experiment and simulations as the amount of feedback is increased. A relevant extension of this work would be the evaluation of the scaling at shorter time scales to examine the temporal influence of noise at the inherent time scales of the laser system, as estimated by the Hurst exponent.

In the second experiment we asked the opposite question. That is, at low pump currents where the noise is believed to strongly govern the dynamics of the low-frequency fluctuations regime, can we find deterministic features in the light dynamics which cannot be captured by a stochastic model alone? We utilized the prehistory and posthistory probability distribution functions for the intensity dropouts to find recurrent features in the dynamics. This technique allowed us to detect signatures of chaotic itinerancy in the dynamics of the staircase recovery, that is, the unlocking of the slow carrier dynamics, in experimental and simulated measurements of the light and carrier dynamics. An important consequence of this analysis was the discovery of an itinerant epoch before the intensity dropout occured, giving a strong indication of the deterministic origin of the power dropouts. In the experiment, however, we only looked at a single moderate feedback strength. We could easily ask, then, if the same deterministic signature would remain when the feedback is lowered and noise has a more prevalent role?

Finally, we performed a final experiment which sought the role that noise plays in determining which output is present as the injection current is tuned between the two dominant chaotic regimes. We discovered an intermittency in the light output between the boundary of the LFF and CC states by increasing the injection current. We found that although noise preserves the intermittent transition, it translates the

span of this region to higher injection currents, such that, for high noise levels, the interactions betweeen the external cavity modes which make up the CC dynamics are suppressed. The spontaneous emission therefore plays a large part in guiding the dynamical interactions in this system. In addition, an experimental characterization of the intermittent transition sheds light on the amount of noise which affects the dynamical evolution of the light output in the system.

A majority of studies have approached the irregular light output produced in a semiconductor laser with coherent optical feedback stictly as either a deterministic or stochastic phenomenon. The results of this dissertation imply that noise and coherent feedback must *concurrently* be considered in simulations of the system in order to accurately reproduce the light dynamics and their response to changes in the system parameters. The interactions between the random input of spontaneous emission and deterministic feedack provided by the external cavity in the dynamical evolution of the system is a subject which we have only begun to understand and will provide challenging problems for years to come.

BIBLIOGRAPHY

[1] A. L. Schawlow and C. H. Townes, Phys. Rev. **112**, 1940 (1958).

[2] T. H. Maiman, Nature **187**, 493 (1960).

[3] R. N. Hall, G. E. Fenner, J. D. Kingsley, T. J. Soltys, and R. O. Carlson, Phys. Rev. Lett. **9**, 366 (1962).

[4] N. Holonyak and S. F. Bevacqua, Appl. Phys. Lett. **1**, 82 (1962).

[5] M. I. Nathan, W. P. Dumke, G. Burns, F. H. Dill, and G. Lasher, Appl. Phys. Lett. **1**, 62 (1962).

[6] T. M. Quist, R. H. Rediker, R.J. Keyes, W. E. Krag, B. Lax, A. L. McWhorter, and H. J. Zeiger, Appl. Phys. Lett. **1**, 91 (1962).

[7] *Laser Focus World* **40**, Jan. (2004), p.75.

[8] G. P. Agrawal and N. K. Dutta, *Semiconductor Lasers*, 2nd ed., Kluwer Acadamic Publishers, Massachusetts (1993).

[9] L. A. Coldren and S. W. Corzine*Diode Lasers and Photonic Integrated Circuits*, Wiley, New York (1995).

[10] G. R. Gray and R. Roy, J. Opt. Soc. Am. B (Optical Physics), **40**, 632 (1991).

[11] *Laser Electronics*, Prentice Hall, New Jersey (1989).

[12] C. H. Henry, IEEE J. Quantum Electron. **QE-18**, 259 (1982).

[13] M. C. Mackey and L. Glass, Science **197**, 287 (1977).

[14] N. MacDonald *Biological Delay Systems: Linear Stability Theory*, Cambridge University Press, Cambridge (1989).

[15] J. D. Farmer, Physica, **4D**, 366 (1982).

[16] K. Tsuka and J. L. Chern, Opt. Lett. **16**, 1759 (1991).

[17] C. H. Lee and S. Y. Shin, Appl. Phys. Lett. **62**, 922 (1993).

[18] Y. Cho and T. Umeda, Opt. Commun. **59**, 131 (1986).

[19] R. W. Tkach, and A. R. Chraplyvy, Electron. Lett. **21**, 1081 (1985).

[20] E. Patzak, H. Olesen, A. Sadimura, S. Saito and T. Mukai, Electron. Lett. **19**, 938 (1983).

[21] G. P. Agrawal, IEEE J. Quantum Electron. **QE-20**, 4689 (1984).

[22] R. O. Miles, A. Dandridge, A. B. Tveten, H. F. Taylor and T. G. Giallorenzi, Appl. Phys. Lett **37**, 990 (1980).

[23] R. Lang and K. Kobayashi, IEEE J. Quantum Electron. **QE-16**, 347 (1980).

[24] K. Kaneko and I. Tsuda, editors, *Chaotic Itinerancy*, focus issue, Chaos **13**, 926 (2003).

[25] K. Kaneko, Physica D **41**, 137 (1990); I. Tsuda, World Futures **32**, 167 (1991).

[26] K. Ikeda, K. Otsuka, and K. Matsumoto, Prog. Theor. Phys. Suppl. **99**, 295 (1989).

[27] Z. Hong, L. Yaowen, W. Yinghai, and H. Bambi, Phys. Rev. E **58**, 4383 (1998).

[28] F. T. Arecchi, G. Giacomelli, P. L. Ramazza, and S. Residori, Phys. Rev. Lett. **65**, 2531 (1990).

[29] K. Otsuka *et al.*, Chaos **13**, 1014 (2003).

[30] I. Fischer *et al.*, Phys. Rev. Lett. **76**, 220 (1996).

[31] W. S. Lam, P. N. Guzdar, R. Roy, Phys. Rev. E **67**, 025604(R) (2003).

[32] H. E. Hurst, R. P. Black, and Y. M. Simaika, *Long-Term Storage: An Experimental Study*, Constable, London (1965).

[33] B. B. Mandelbrot, *Fractal Geometry of Nature*, W H Freeman, New York (1982).

[34] M. I. Dykman *et al.*, Phys. Rev. Lett. **68**, 2718 (1992).

[35] J. Hales, A. Zhukov, R. Roy, and M. I. Dykman, Phys. Rev. Lett., **85**, 78 (2000).

[36] L. Gammaitoni, P. Hänggi, P. Jung and F. Marchesoni, Rev. Mod. Phys. **70**, 223 (1998).

[37] A. S. Pikovsky and J. Kurths, Phys. Rev. Lett. **78**, 775 (1997).

[38] S. Kim, S. H. Park and C. S. Ryu, Phys. Rev. Lett. **78**, 1616 (1997).

[39] K. Kaneko, Phys. Rev. Lett. **78**, 2736 (1997).

[40] S. Kraut, U. Feudel and C. Grebogi, Phys. Rev. E **59**, 5253 (1999).

[41] P. Spencer, P. Rees, and I. Peirce, *Unlocking Dynamical Diversity: Optical Feedback Effects on Semiconductor Lasers*, edited by D. M. Kane and K. A. Shore, p. 23, Wiley, West Sussex (2005).

[42] W. H. Press, W. T. Vetterling, S. A. Teukolsky and B. P. Flannery *Numerical Recipes in C*, Cambridge Univ. Press, Cambridge (1999).

[43] P. M. Alsing, V. Kovanis, A. Gavrielides and T. Erneux, Phys. Rev. A **53**, 4429 (1996).

[44] B. Tromborg, J. H. Osmundsen, and H. Olesen, IEEE J. Quantum Electron. **QE-20**, 1023 (1984).

[45] J. Mørk, B. Tromborg and J. Mark, IEEE J. Quantum Electron. **QE-28**, 93 (1992).

[46] J. Mørk, J. Mark, and B. Tromborg, Phys. Rev. Lett. **65**, 1999 (1990).

[47] C. Masoller and N. B. Abraham, Phys. Rev. A **57**, 1313 (1998).

[48] C. H. Henry and R. Kazarinov, IEEE J. Quantum Electron. **QE-22**, 294 (1986).

[49] T. Heil, I. Fischer, and W. Elsäßer, Phys. Rev. A **60**, 634 (1999).

[50] D. Lenstra, B. H. Verbeek, and A. J. Den Boef, IEEE J. Quantum Electron. **QE-21**, 674 (1985).

[51] T. Sano, Phys. Rev. A **50**, 2719 (1994).

[52] D. Gabor, J. IEE (London) **93**, 429 (1946); M. Born and E. Wolf, *Principles of Optics*, 7th ed., pp. 557-562, Cambridge University Press, New York (1999).

[53] M. G. Rosenblum, A. S. Pikovsky, and J. Kurths, Phys. Rev. Lett. **76**, 1804 (1996).

[54] A. S. Pikovsky, M. G. Rosenblum, and J. Kurths, *Synchronization: A Universal Concept in Nonlinear Sciences*, Cambridge University Press, Cambridge (2001).

[55] T. Yalçinkaya and Y.C. Lai, Phys. Rev. Lett. **79**, 3885 (1997).

[56] N. E. Huang *et. al.*, Proc. Roy. Soc. (London) **454**, 903 (1998).

[57] J. Feder, *Fractals*, Ch. 8 and 9, Plenum Press, New York (1988).

[58] W. S. Lam, W. Ray, P. N. Guzdar and R. Roy, Phys. Rev. Lett. **94**, 010692 (2005).

[59] P. S. Addison, *Fractals and Chaos*, p. 54, Institute of Physics Publishing, London (1997).

[60] W. S. Lam, P. N. Guzdar and R. Roy, Phys. Rev. E **67**, 25604 (2003).

[61] D. Deshazer, R. Breban, E. Ott, and R. Roy, Phys. Rev. Lett. **87**, 044101 (2001).

[62] Y. C. Lai and N. Ye, Int. J. Bif. Chaos **13**, 1383 (2003).

[63] N. E. Huang, *Hilbert-Huang Transform and Its Applications*, editors N. E. Huang and S. S. P. Shen, p. 1, World Scientific Publishing Co. Pte. Ltd., Singapore (2005).

[64] N. E. Huang *et. al.*, Proc. Roy. Soc. (London) **459**, 2317 (2003).

[65] P. Flandrin, G. Rilling and P. Goncalves, IEEE Sig. Proc. Lett. **11**, 112 (2004).

[66] J. Ohtsubo, Prog. Optics **44**, 1 (2002).

[67] I. Fischer *et al.*, Phys. Rev. Lett. **76**, 220 (1996).

[68] A. Hohl, H. J. C. van der Linden, and R. Roy, Opt. Lett. **20**, 2396 (1995).

[69] D. G. Luchinsky and P. V. E. McClintock, Nature (London) **389**, 463 (1997).

[70] M. H. Devoret, D. Esteve, J. M. Martinis, A. Cleland and J. Clarke, Phys. Rev. B **36**, 58 (1977).

[71] L. Onsager and S. Machlup, Phys. Rev. **91**, 1505, 1512 (1953).

[72] G. Huyet *et al.*, Europhys. Lett. **40**, 619 (1997); S. P. Hegarty, G. Huyet, P. Porta, and J. G. McInerney, Opt. Lett. **23**, 1206 (1998).

[73] Y. Liu, P. Davis, and Y. Takiguchi, Phys. Rev. E **60**, 6595 (1999).

[74] R. Ries and F. Sporleder, in *Proceedings of the 8th European Conference on Optical Communication, Cannes, France, 1982* (Comité de la Confe-graverence Européenne sur les Communications Optiques, Cannes, 1982), p. 285; as referenced in K. Petermann, *Laser Diode Modulation and Noise* (Kluwer, Dordrecht, 1988), p. 281.

[75] C. Risch and C. Voumard, J. Appl. Phys. **48**, 2083 (1977).

[76] W. S. Lam, *Nonlinear Dynamics of Semiconductor Lasers with Optical Feedback*, Ph.D. Thesis, University of Maryland, MD (2003).

[77] T. Heil, I. Fischer, and W. Elsäßer, Phys. Rev. A **58**, 2672 (1998).

[78] J. Mulet and C. R. Mirasso, Phys. Rev. E **59**, 5400 (1999).

[79] J. Sacher, W. Elsäßer, and E. O. Göbel, Phys. Rev. Lett. **63**, 2224 (1989).

[80] A. M. Levine, G. H. M. van Tartwijk, D. Lenstra, and T. Erneux, Phys. Rev. A **52** R3436 (1995).

[81] R. Meucci, E. Allaria, F. Salvadori, and F. T. Arecchi, Phys. Rev. Lett. **95**, 184101 (2005).